The Astrophysical Journal Supplement Series, 246:7 (20pp), 2020 January https://doi.org/10.3847/1538-4365/ab5b97

A Large-scale ^{12}CO, ^{13}CO, and C^{18}O Molecular Cloud Survey in the Outer Galactic Plane over $l = [129.^{\circ}75, 140.^{\circ}25]$ and $b = [-5.^{\circ}25, +5.^{\circ}25]$

Yan Sun, Ji Yang, Ye Xu, Shaobo Zhang, Yang Su, Hongchi Wang, Xue-Peng Chen, Deng-Rong Lu, Ji-Xian Sun, Bing-Gang Ju, Yong-Xing Zhang, Xin Zhou, and Zhi-Bo Jiang
Purple Mountain Observatory and Key Laboratory of Radio Astronomy, Chinese Academy of Sciences, Nanjing 210034, People's Republic of China
yansun@pmo.ac.cn
Received 2019 July 1; revised 2019 November 22; accepted 2019 November 24; published 2020 January 6

Abstract

We present the data of an unbiased $J = 1$–0 ^{12}CO/^{13}CO/C^{18}O survey of molecular clouds in the Galactic plane over $l = [129.^{\circ}75, 140.^{\circ}25]$ and $b = [-5.^{\circ}25, +5.^{\circ}25]$. For the full $10.^{\circ}5 \times 10.^{\circ}5$ region sampled at 30″, there are 1,590,120 spectra for each isotopologue. The high sensitivity and large spatial dynamic range of the maps provide valuable insights into the structure, physical properties, and kinematics of the molecular gas. The new data successfully trace the most distant spiral arm, as well as the internal subfeatures of the nearby spiral arms. The combined data set of ^{12}CO, ^{13}CO, and C^{18}O allows us to make a more accurate inventory of gas column density and mass for molecular gas within this Galactic interval than hitherto attempted. A statistical analysis reveals that a large fraction of the observed molecular gas is emitted from regions with low excitation conditions. As expected, a considerable amount of H_2 mass is found to be confined to the spiral arms. Moreover, we find that the C^{18}O emission is exclusively seen along spiral arms at current detection limits. The physical properties of molecular gas vary considerably in different spiral arms and inter-arms. We find that the column density probability density functions and the amount of relatively denser gas (traced by ^{13}CO or C^{18}O) appear to be closely related to the level of massive star formation activity within the molecular gas. The high-quality data also reveal that the warp and flare of the Galactic plane become obvious beyond the Perseus arm in this Galactic longitude range.

Unified Astronomy Thesaurus concepts: Galaxy structure (622); Interstellar medium (847); Star formation (1569); Molecular clouds (1072); Surveys (1671); CO line emission (262)

1. Introduction

Molecular gas, an important component of the interstellar medium, exists within a wide range of environmental conditions. The molecular star-forming gas is generally concentrated in giant molecular clouds (GMCs), with masses 10^4–10^6 $M_{\odot}$ and above, while diffuse gas exists in low-density or low-column-density regions. Furthermore, observations of external spiral galaxies, such as M51, have revealed that the star-forming molecular gas is concentrated along spiral arms (e.g., Koda et al. 2009; Schinnerer et al. 2013). As one of the most abundant molecular species, CO has been the most widely used tracer of H_2 since its discovery by Wilson et al. (1970) and also provides excellent diagnostics of line-of-sight motions and temperatures. Because of its great abundance and hence high optical depth, ^{12}CO is effective in probing the total molecular gas, including the diffuse outer envelopes of the molecular clouds with a density of $\sim 10^2\,\mathrm{cm}^{-3}$. On the other hand, because of their lower abundance and hence lower optical depth, ^{13}CO and C^{18}O can probe deeper into the envelopes and trace the much higher column density regions, with a typical density of $\sim 10^3$–$10^4\,\mathrm{cm}^{-3}$ (e.g., Umemoto et al. 2017). Therefore, the combination of the multispecies CO molecular lines will allow us to probe molecular gas in a variety of regimes of column or volume density, and thus will greatly improve our knowledge of the structure and properties of the molecular gas.

Aiming to provide a full overview of the distribution of molecular gas across the Galactic plane, many unbiased CO surveys have been conducted using single-dish telescopes, which were summarized in a recent review paper by Heyer & Dame (2015). Among them, the majority of the CO surveys only cover a single species of CO molecular line (whether ^{12}CO or ^{13}CO, e.g., Heyer et al. 1998; Dame et al. 2001; Lee et al. 2001; Mizuno & Fukui 2004; Jackson et al. 2006), and a few of them cover the multispecies CO molecular lines (^{12}CO, ^{13}CO, and/or C^{18}O, e.g., Ridge et al. 2006; Narayanan et al. 2008; Barnes et al. 2015; Umemoto et al. 2017; Barnes et al. 2018).

The ongoing project Milky Way Imaging Scroll Painting (MWISP) is an unbiased $J = 1$–0 ^{12}CO/^{13}CO/C^{18}O survey of the Northern Galactic Plane (refer to Zhang et al. 2014; Du et al. 2017; Sun et al. 2017; Su et al. 2019, etc., for project details and initial results). As part of the MWISP survey, the Galactic region of $l = [129.^{\circ}75, 140.^{\circ}25]$ and $b = [-5.^{\circ}25, +5.^{\circ}25]$ (hereafter the G130 region) has been completely covered. A rich collection of objects lies in this region, containing one of the most famous molecular cloud associations (W3–W4–W5), three newly formed, massive star associations (IC 1795, IC 1805, and IC 1848), as well as a number of supernova remnants (SNRs) and young H II regions. Therefore, this region has been comprehensively studied at a variety of wavelengths from millimeter and submillimeter to X-ray (e.g., Heyer et al. 1998; Carpenter et al. 2000; Kramer et al. 2004; Moore et al. 2007; Sakai et al. 2007; Ruch et al. 2007; Feigelson & Townsley 2008). The most extensive inventory of the molecular gas content within this Galactic range was conducted by the Harvard-Smithsonian Center for Astrophysics (CfA) 1.2 m telescope (Lada et al. 1978; Digel et al. 1996) and the Five College Radio Astronomy Observatory (FCRAO) 14 m telescope (Heyer et al. 1998), which only observed emission from the main ^{12}CO molecular line. However, the relatively low

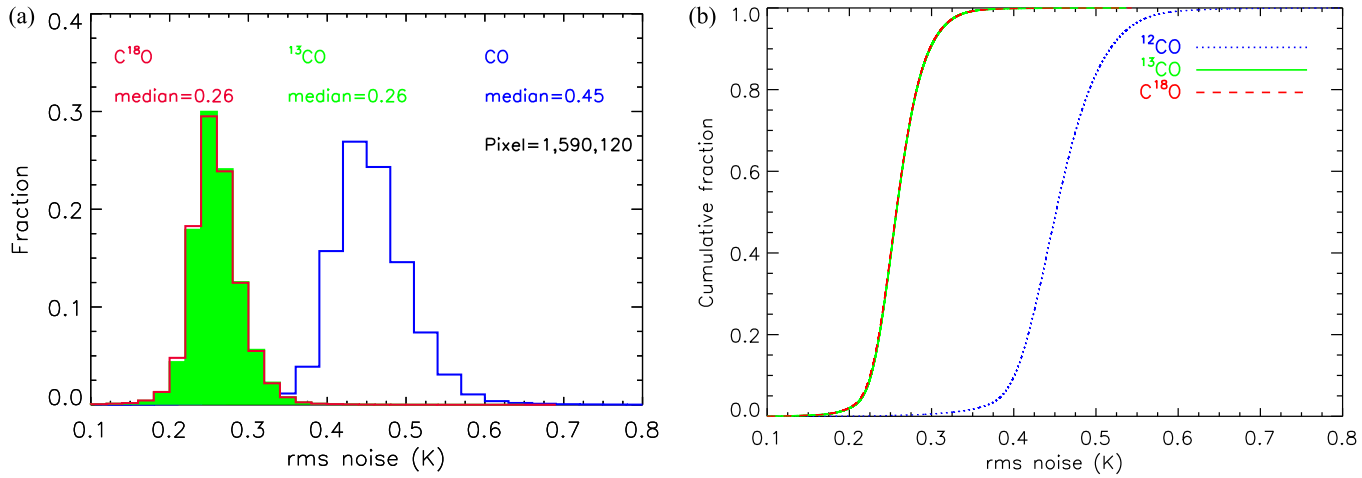

Figure 1. (a) Histograms of σ for each isotopologue. (b) Cumulative distributions of σ for each isotopologue.

sensitivities of these surveys and the optically thick nature of ^{12}CO preclude an examination of the underlying structure of the molecular gas. We should also note that the regions with Galactic latitude $b < -3°$ were not covered by the FCRAO survey. To date, CO and its rare isotopologue observations were only focused on some targeted GMCs rather than the entire scope of the G130 region (e.g., Bieging & Peters 2011; Polychroni et al. 2012).

In this paper, we present the results of the MWISP ^{12}CO/^{13}CO/C^{18}O survey for the G130 region. First, the observations and data reduction strategies are presented in Section 2, and in Section 3 the derivations of the column density and mass of molecular gas are presented along with a discussion of their distributions in different portions of the G130 region. Next, in Section 4, we investigate the current massive star-forming sites in the region, and we discuss the relationships between the molecular gas properties and the level of star formation activity. In Section 5 the warp and flare of the outer Galactic disk revealed by the vertical distribution of molecular gas are presented. In Section 6 we summarize the results.

2. Observations

The observations were conducted during 2011 to 2017 November using the 13.7 m millimeter-wavelength telescope of the Purple Mountain Observatory (PMO) in Delingha, China, at an altitude of about 3200 m. The Superconducting Spectroscopic Array Receiver, a nine-beam, sideband-separating (~10 dB of sideband rejection) receiver, was used as the front end. Nine beams are aligned on a square $6' \times 6'$ grid with ~3′ spacing, and the beam size is ~50″ at 115 GHz. The back-end system comprises 18 fast Fourier transform spectrometers, each configured with 1 GHz bandwidth (61 kHz frequency resolution) and 16,384 spectral channels, which yield velocity resolutions of 0.158 km s^{-1} at 115 GHz and 0.167 km s^{-1} at 110 GHz and a velocity coverage of ~2600 km s^{-1}. The standard chopper wheel calibration was used during the observation to get the antenna temperature, T_A^*. The pointing accuracy was better than 5″ in the observing epoch. The molecular lines of ^{12}CO(J = 1–0) in the upper sideband and ^{13}CO(J = 1–0) and C^{18}O(J = 1–0) in the lower sideband were observed simultaneously. The typical noise temperatures including the atmosphere at 110 GHz and 115 GHz are 140 K and 250 K, respectively. A detailed description of the instrument was given by Shan et al. (2012).

Regions within the Galactic coordinate ranges of l = [129.°75, 140.°25] and b = [−5.°25, 5.°25] were divided into 441 patches in an (l, b) grid for mapping, each with a size of $30' \times 30'$. The on-the-fly (OTF) mode was applied. The typical scan rate and dump time are 50 (or 75) ″/s and 0.3 (or 0.2) s. These setups result in a sample spacing of 15″ between adjacent scans, fulfilling the oversampling of the ~50″ beam of the 13.7 m telescope (see the details in Sun et al. 2018; Su et al. 2019). Each patch with a dimension of $30' \times 30'$ has been scanned along two directions, which have a 0° and a 90° position angle with respect to the Galactic latitude axis, respectively. Thus, each position on the sky was observed at least in two independent maps of different position angles, greatly reducing many systematic effects (e.g., striping in the scanning direction). The nominal sensitivities of the survey are set to be 0.3 K in ^{13}CO/C^{18}O at a channel width of 0.17 km s^{-1}, and 0.5 K in ^{12}CO at a channel width of 0.16 km s^{-1}. In some limited regions, much higher sensitivities of 200 and 100 mK were achieved, aiming to better confine molecular outflows in those regions. The instrument was checked every 2–3 hr by observing the nearby strong standard sources, S140 and W3(OH).

The CLASS program contained in the GILDAS software package[1] (Pety 2005) was used for our data reduction. A first-order baseline was applied to the spectra in this survey, and the spectra channels were not smoothed in this study. The OTF raw data were regridded into 30″ × 30″ pixels and converted to a FITS cube. All of the 441 small maps were added together to create the final large mosaic, which contains about 1,590,120 spectra in each isotopologue. Data presented here are on the main beam brightness temperature scale ($T_{\rm mb}$), corrected for beam efficiencies, using $T_{\rm mb} = T_{\rm A}^* / \eta_{\rm mb}$, where $\eta_{\rm mb}$ was typically 0.51 for ^{13}CO and C^{18}O and 0.46 for ^{12}CO (see the status report of the telescope[2]).

The histograms in Figure 1 show the normalized number distributions of $\sigma(T_{\rm R}^*)$ for ^{12}CO in blue, ^{13}CO in green, and C^{18}O in red. The median rms noise level of the spectra is 0.45 K for ^{12}CO at a channel width of 0.16 km s^{-1} and 0.26 K for ^{13}CO

[1] http://www.iram.fr/IRAMFR/GILDAS
[2] http://www.radioast.nsdc.cn/mwisp.php

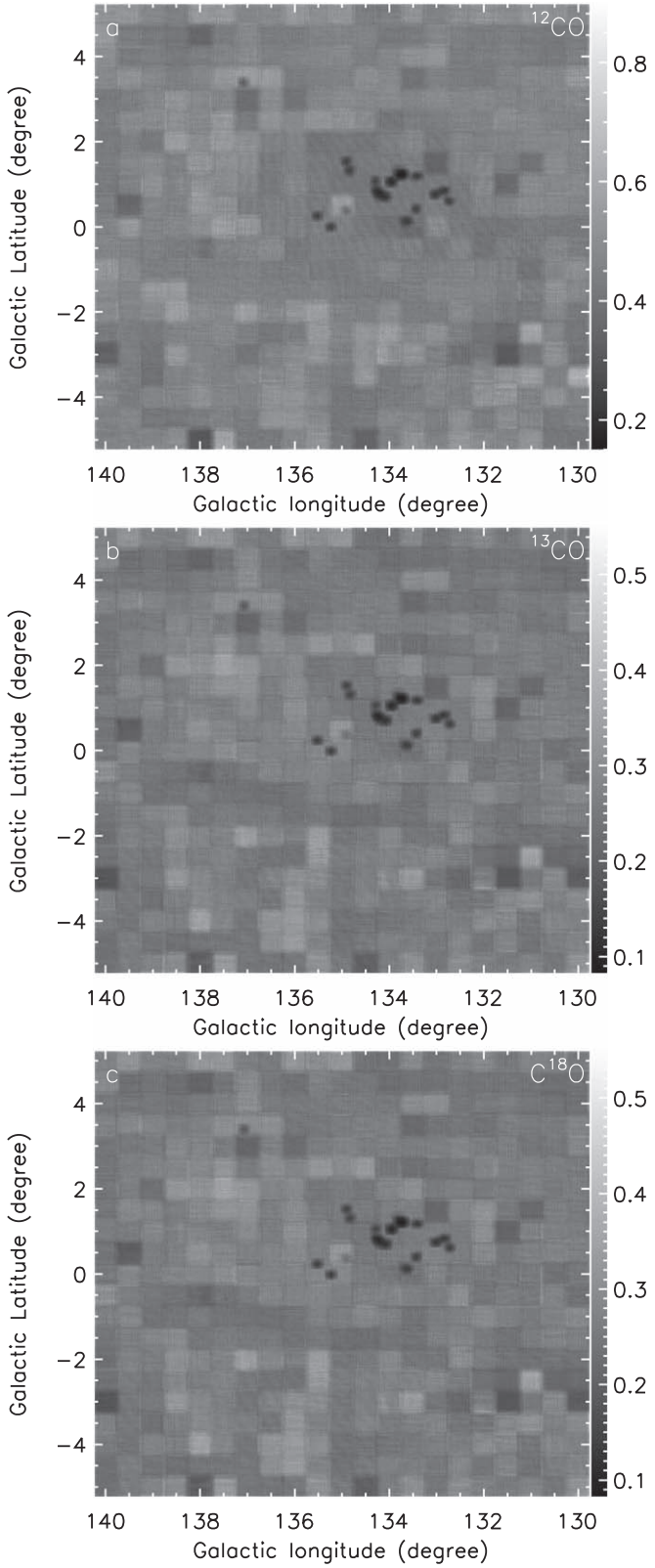

Figure 2. The rms noise maps for each isotopologue. In the black dot regions, much higher sensitivities of ∼200 mK (^{12}CO) and ∼100 mK (^{13}CO and ^{13}CO) were achieved, aiming to better confine molecular outflows in those regions.

and C^{18}O at a channel width of 0.17 km s^{-1}. Figure 2 shows the $\sigma(T_R^*)$ maps of each isotopologue, which cover approximately 110 deg^2 on the sky. All three isotopologues show near-uniform sensitivity over most of the field. Since ^{13}CO and C^{18}O are very close in frequency and were both received in the lower sideband, they show very similar rms noise.

3. Parameters of Large-scale Structures

3.1. Large-scale Structure Traced by ^{12}CO/^{13}CO/C^{18}O

Figure 3 shows the *l*–*v* and *b*–*v* maps of the CO emission, by obtaining average emission over $b = -5.^\circ25$ to $5.^\circ25$ and $l = 129.^\circ75$ to $140.^\circ25$, respectively. In this direction, Galactic rotation causes radial velocity to become more negative with increasing distance. Constant Galactocentric radii of 10, 13, 16, and 19 kpc (calculated under the assumption of a rotation curve from Reid et al. 2014, hereafter the Reid rotation curve) are indicated with dashed lines. Note that to improve the signal-to-noise ratio in the maps, only those pixels with at least three contiguous channels above 3σ are averaged. We break the data up into three regions, according to the detection or nondetection of ^{12}CO, ^{13}CO, and C^{18}O emission. Then we define mask "B," "G," and "R" to be the regions where ^{12}CO, ^{13}CO, and C^{18}O emission exists, respectively. In fact, the R region also contains ^{13}CO and ^{12}CO emission, and the "G" region also contains ^{12}CO emission. This means that the mask "R" region (in red color in Figure 3) is included in the mask "G" region (in red and green in Figure 3), which is further included in the mask "B" region (in red, green, and blue in Figure 3). In the *l*–*v* map, some coherent, large-scale structures are apparent, which have long been recognized as spiral arms (e.g., Weaver 1974; Dame et al. 1986). As mentioned above, this region was fully covered by the 1.2 m telescope CO survey, by which only the two nearby arms, the Local and Perseus arms, were well traced, and very little emission beyond the Perseus arm was detected (refer to the *l*–*v* map in Digel et al. 1996).

It is intriguing that the new high-resolution data enable us to well resolve at least two substructures within the velocity ranges of the two relatively nearby arms (the Local arm [−20, 7 km s^{-1}] and the Perseus arm [−63, −30 km s^{-1}]), and even within the distant Outer arm [−88, −68 km s^{-1}]. These substructures are parallel in most longitude intervals and appear to twist together in certain longitude directions (in Figure 3(a)). The substructures along ∼−3 and ∼−11 km s^{-1} within the Local arm were also detected by the 1.2 m telescope ^{12}CO survey, but show more separated substructures by our new ^{13}CO data. These substructures have been known to be associated with the Gould Belt and the Cam OB1 (Digel et al. 1996). Similar substructures along ∼−40 and ∼−50 km s^{-1} within the Perseus arm are first resolved by the new data with improved resolution. We should note that the molecular gas component of the Outer arm appears as a clear and distinct feature in both the *l*–*v* and *b*–*v* maps for the first time. This arm also seems to contain two substructures along ∼−72 and −79 km s^{-1}. A weak component lying beyond the Outer arm at the maximum negative velocity is also visible, which was interpreted as emission possibly from the Outer Scutum Centaurus (OSC) arm (Sun et al. 2015). Between each pair of adjacent arms, molecular gas is much poorer in the inter-arm regions than in the spiral arms.

To better define the velocity range of each arm and inter-arm, the LSR velocity distribution of the G130 region is also plotted as a histogram in Figure 4. The blue, green, and red colors indicate the distribution of ^{12}CO, ^{13}CO, and C^{18}O emission. It can be seen that the two velocity V_{lsr} components with significant emission are from the two relatively nearby arms. The multiple V_{lsr} peaks correspond to the substructures mentioned

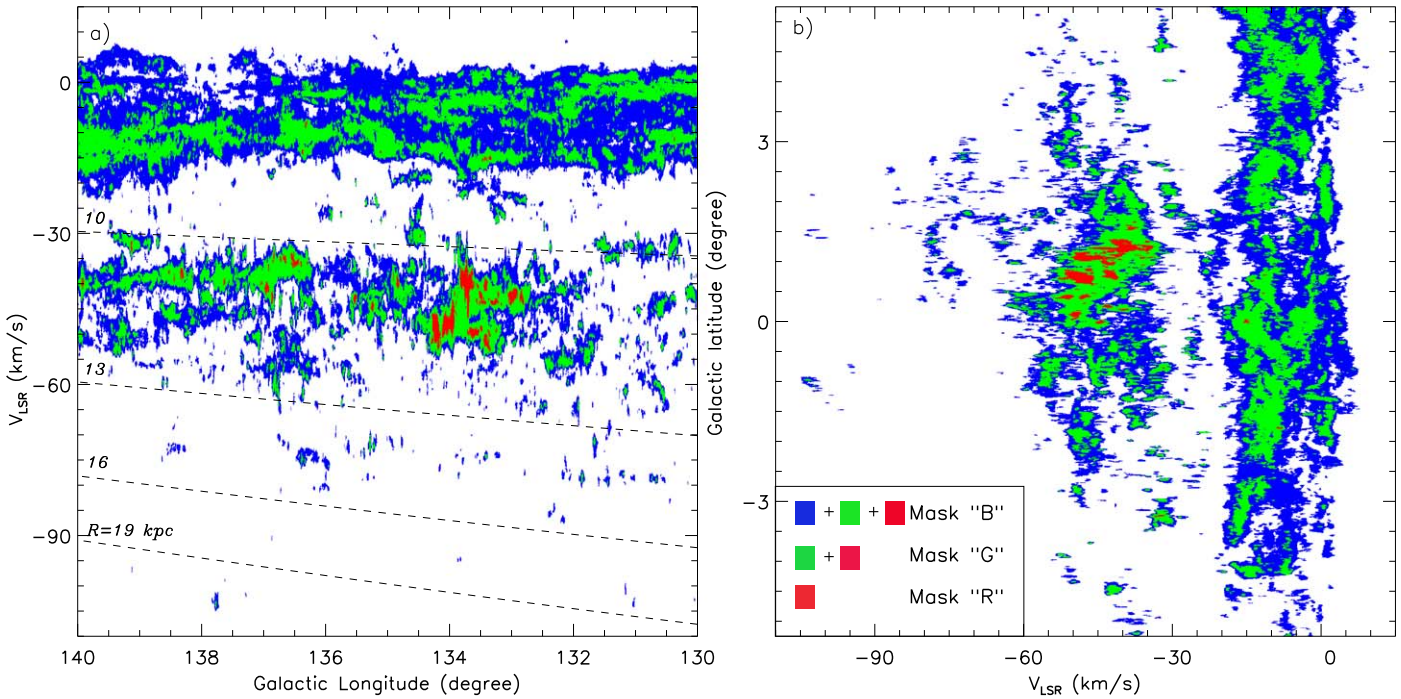

Figure 3. (a): Longitude–velocity map of the entire field, integrated over latitudes $b = -5.^{\circ}25$ to $+5.^{\circ}25$. The dashed lines indicate constant Galactocentric distances of 10, 13, 16, and 19 kpc, calculated under the assumption of the rotation curve from Reid et al. (2014). (b) Latitude–velocity diagram of the entire field, integrated over longitudes $l = 129.^{\circ}75$–$140.^{\circ}25$. The blue, green, and red colors in both maps indicate the regions exhibiting ^{12}CO , ^{13}CO, and C^{18}O emission, respectively, as described in the text.

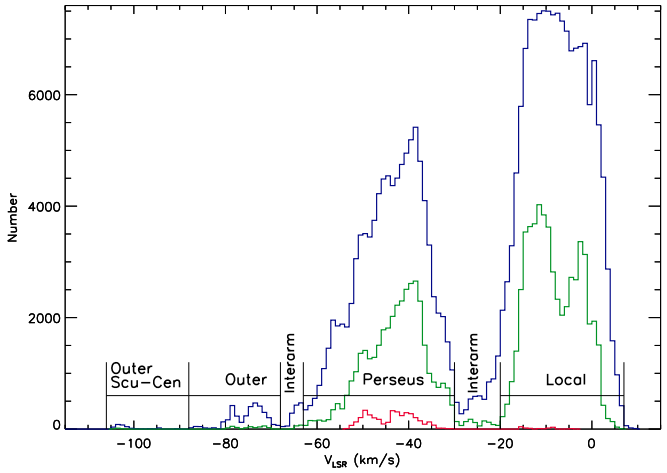

Figure 4. LSR radial velocity distributions of each isotopologue, derived from Figure 3(a).

above. We define the velocity ranges of these two arms as regions with prominent ^{13}CO emission, while the velocity $V_{\rm lsr}$ ranges of the two distant arms are defined by the ranges with prominent ^{12}CO emission. Two very deep and empty inter-arm holes between the Local, Perseus, and Outer arms are apparent. Because of the degeneracy of the radial velocity, the definition of the inter-arm between the Outer and OSC arms is very difficult. Besides, due to the large distance involved, the contribution from the inter-arm becomes negligible. Therefore, the detected CO emission in the extreme outer Galaxy is thought to be exclusively confined to spiral arms rather than inter-arms. The velocity ranges of each arm and inter-arm are indicated in Figure 4 and Table 1.

Table 1
Layers and Mask Regions

Layer Name	V Range (km s^{-1})	Mask Region	Pixel Number	Pixel Percentage	Area (pc^2)
Local	[−20, 7]	B	567, 591	35.7%	4323
		G	69, 003	4.3%	526
		R	52	0.003%	1
Interarm1	[−30, −20]	B	7579	0.44%	263
		G	634	0.04%	22
Perseus	[−63, −30]	B	125, 103	7.9%	10, 166
		G	31, 857	2.0%	2, 588
		R	1, 544	0.1%	125
Interarm2	[−68, −63]	B	1199	0.074%	401
		G	59	0.004%	20
Outer	[−88, −68]	B	3591	0.208%	2725
		G	124	0.008%	94
OSC	[−106, −88]	B	352	0.021%	1258
		G	14	0.001%	50

Similarly, we also define the mask "B," mask "G," and mask "R" regions in the integrated intensity maps for each velocity component (Figure 5). Also, the detection thresholds are 3σ. We find that ^{12}CO and ^{13}CO emission is detected in all velocity structures, while C^{18}O emission is detected in only two velocity structures (the Local arm and the Perseus arm). The different regions and the number of pixels in each velocity component are given in Table 1. Furthermore, the pixel percentage, defined as the ratio of pixel number in one mask to the total pixel number in the entire map (1,590,120 pixels; see Section 2), is also listed in

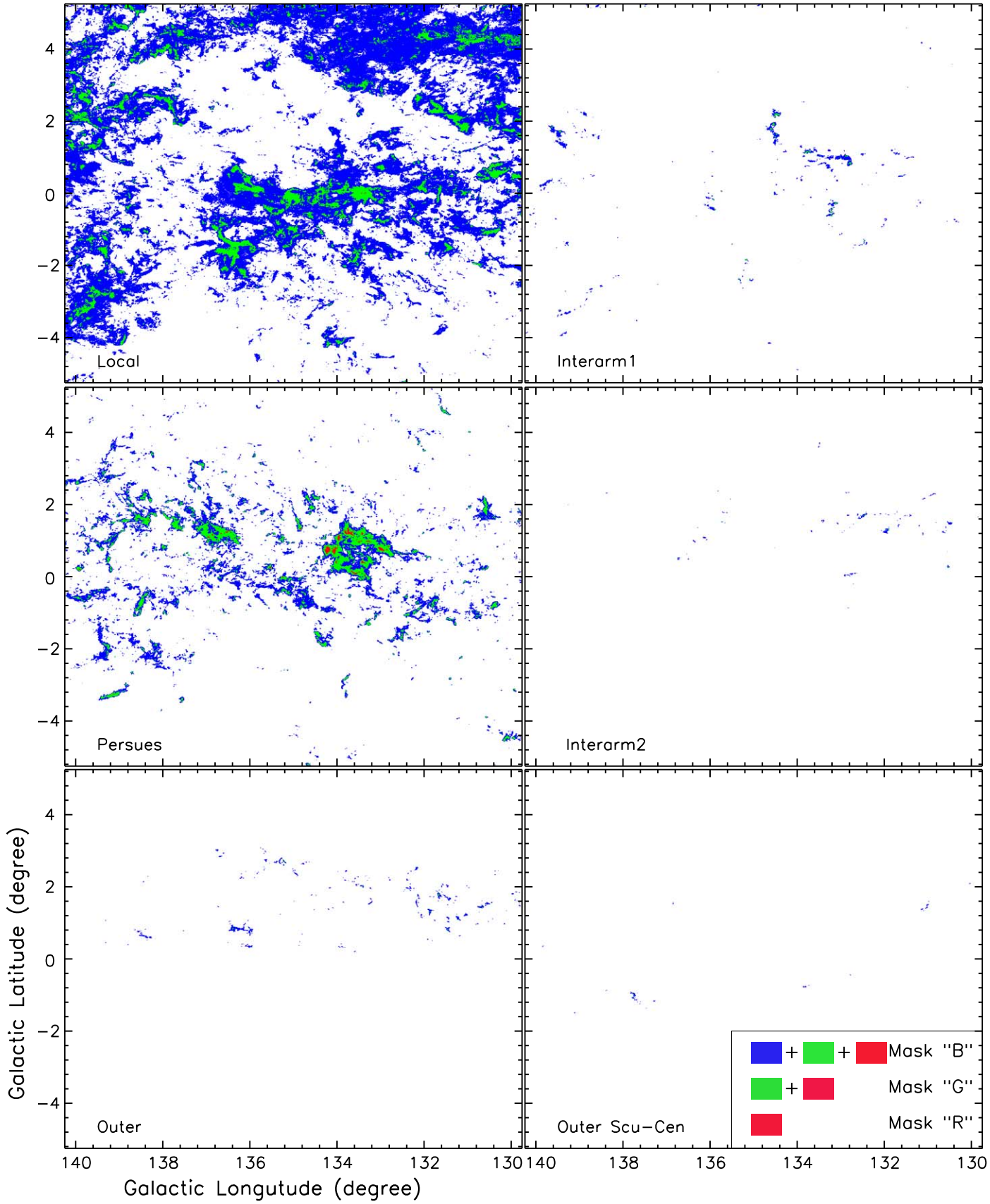

Figure 5. Mask regions of each spiral arm and inter-arm defined in Figure 4. The blue, green, and red colors in each map indicate the regions exhibiting ^{12}CO , ^{13}CO, and C^{18}O emission, respectively, as described in the text.

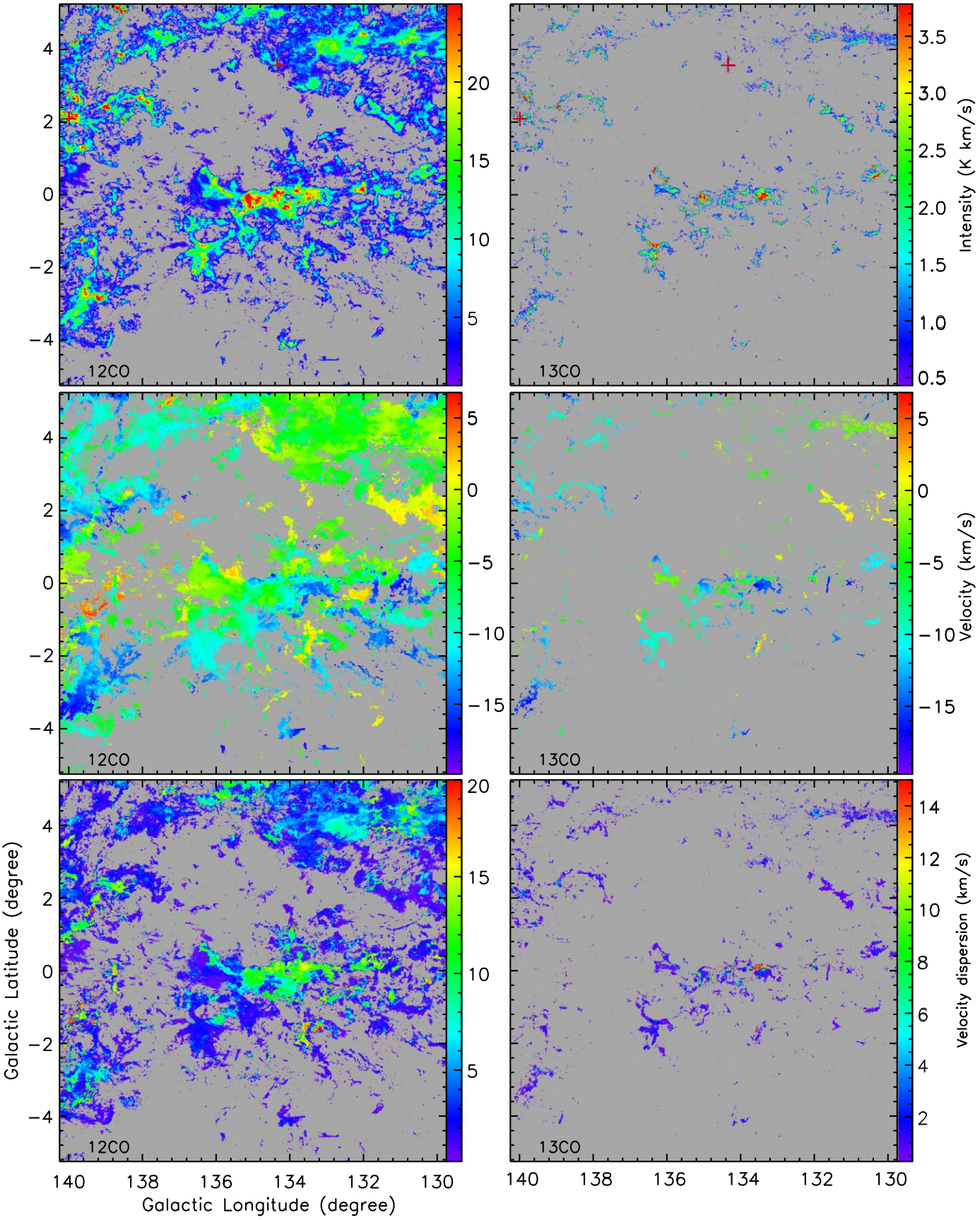

Figure 6. Moment maps (intensity, velocity, and velocity dispersion maps) of ^{12}CO and ^{13}CO emission from the Local arm ($V_{\rm LSR} = -20$ to 7 km s^{-1}). The positions of the known water masers, methanol masers, relatively evolved H II regions, and young H II regions are marked with white crosses, white squares, red pluses, and white pluses, respectively.

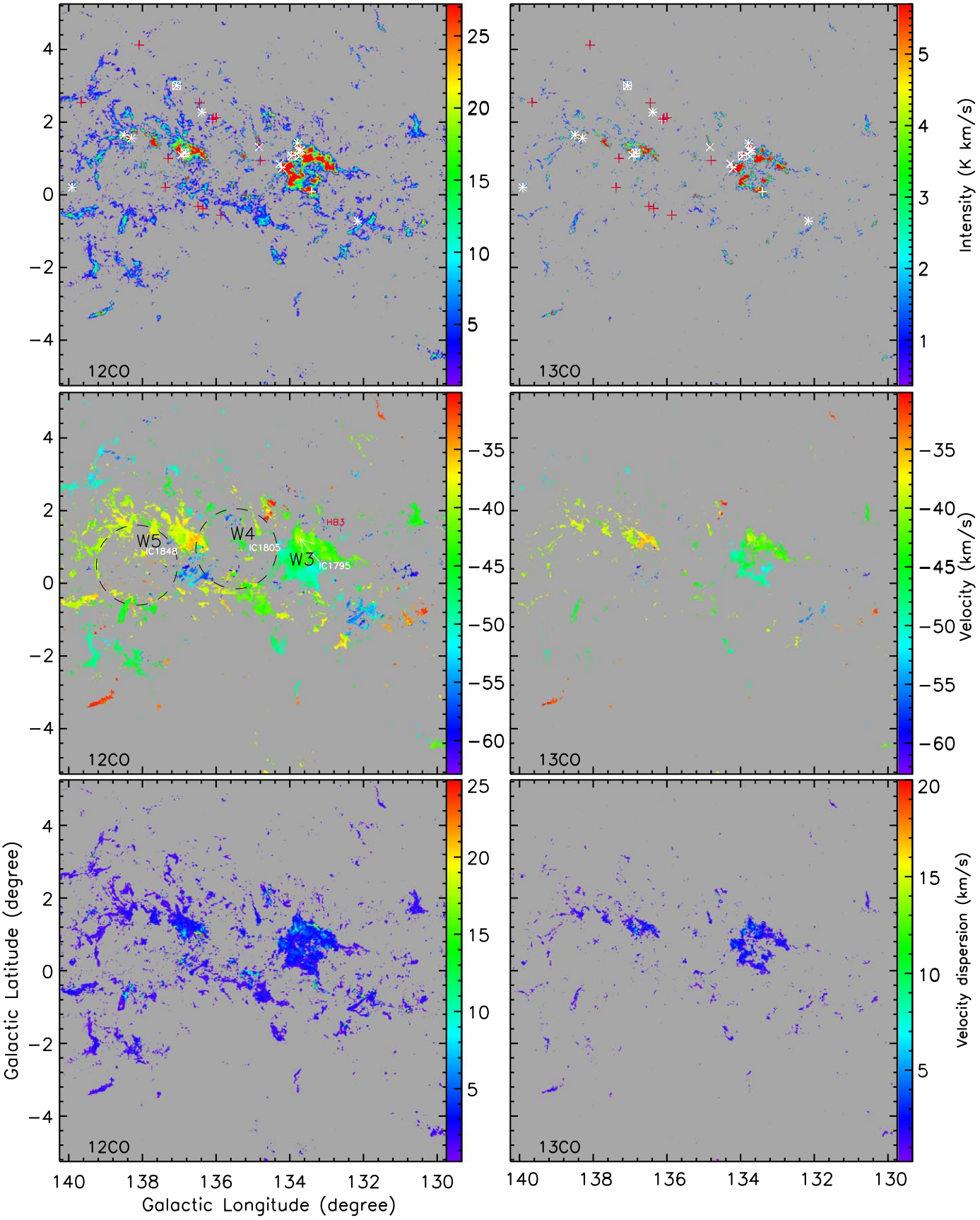

Figure 7. Moment maps of ^{12}CO and ^{13}CO emission from the Perseus arm ($V_{\rm LSR} = -63$ to -30 km s^{-1}). The positions of the known water masers, methanol masers, relatively evolved H II regions, and young H II regions are marked with white crosses, white squares, red pluses, and white pluses, respectively. Famous molecular cloud complexes (W3, W4, and W5), massive star associations (IC 1795, IC 1805, and IC 1848), and the supernova remnant (HB 3) are indicated.

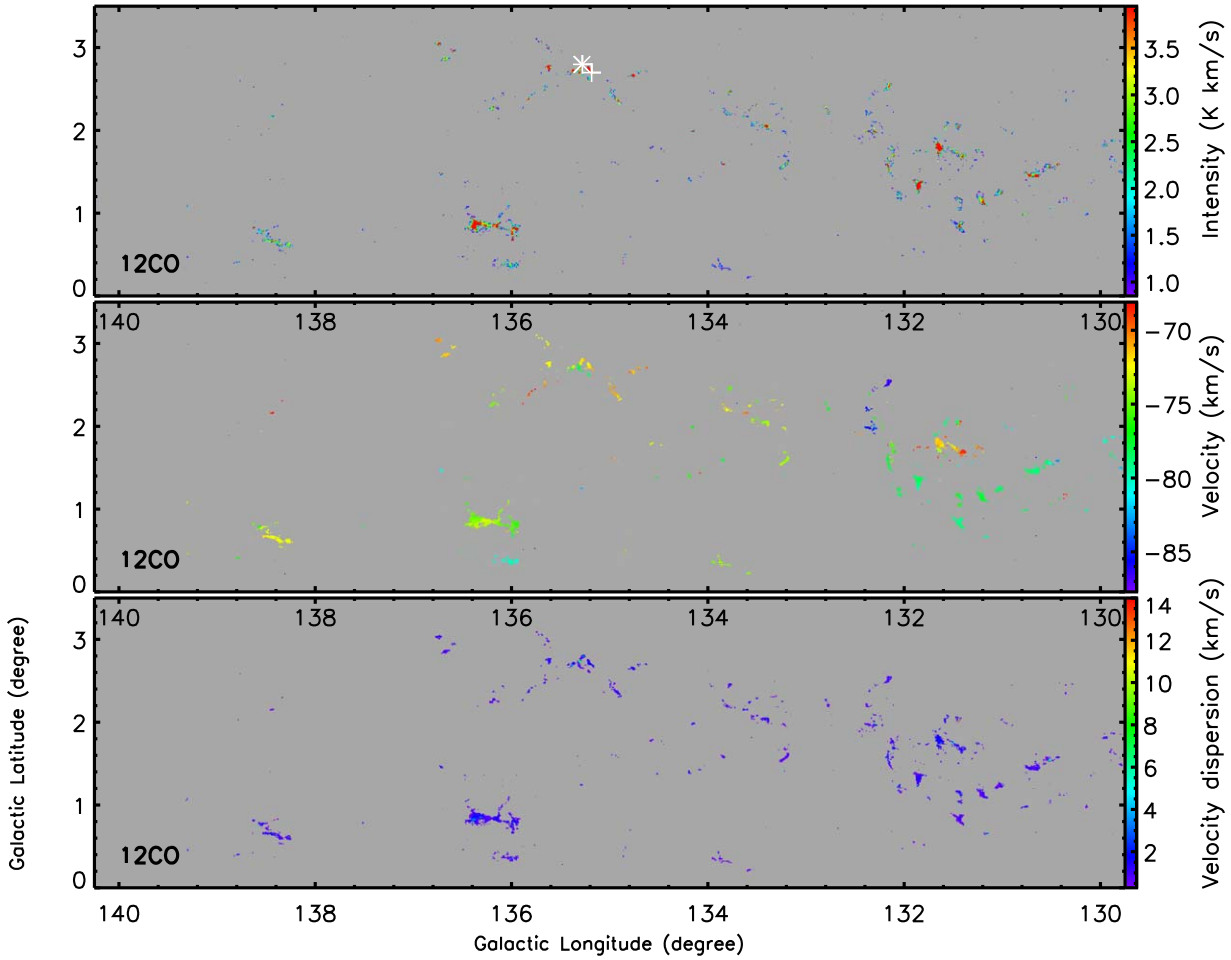

Figure 8. Moment maps of ^{12}CO emission from the Outer arm ($V_{\rm LSR}$ = −88 to −68 km s^{-1}). The positions of the known water masers, methanol masers, relatively evolved H II regions, and young H II regions are marked with white crosses, white squares, red pluses, and white pluses, respectively.

Table 1 (Column 5). It is obvious that the number of pixels in an individual mask occupies only a small fraction of the map pixels (less than 36%). Therefore, molecular gas in the outer Galaxy is relatively sparse compared to the inner Galaxy, that is, at $l = 25°$–$50°$ (see Figure 6 of Su et al. 2019). The statistics also reveal that the mask "B" region shows the greatest number of pixels, and the mask "R" region shows the lowest number of pixels for all velocity structures. Besides, the number of pixels in a spiral arm is considerably larger than that of the inter-arm. The Local arm has the largest number of pixels in the mask "B" and "G" regions, while the Perseus arm has the largest number of pixels in the mask "R" region. The contributions of individual mask regions in each velocity structure are discussed in more detail in Section 3.5.

Figures 6–8 display the moment maps (intensity, velocity distribution, and velocity dispersion maps) of the molecular gas traced by ^{12}CO and ^{13}CO emission for the three most prominent spiral arms, the Local, Perseus, and Outer arms. At first glance, the morphology and the velocity field are very complex. The data reveal two cavities with diameter of ∼2.°2 in the Perseus arm. The data also reveal many filamentary, shell, ring, and cometary structures in the Local, Perseus, and Outer arms. Velocity gradients along these structures (in particular in the Perseus arm) are apparent. These velocity gradients could be interpreted as both rotation and expansion motions of molecular gas. The feedback from a previous generation of OB stars and SNRs may largely account for the observed gradients of the molecular gas in the Perseus arm, because three central clusters (IC 1795, IC 1805, and IC 1848 in the W3–W4–W5 complex) containing a large previous generation of OB stars and an evolved SNR HB 3 are both located in it. The interaction between the SNR HB 3 and the adjacent molecular cloud W3 was discussed by Zhou et al. (2016). Velocity dispersions of a few km s^{-1} are common in each structure, which are consistent with the typical value for individual MCs. However, in the Local arm, some extended areas show a ^{12}CO velocity dispersion as high as 10–15 km s^{-1}, which is mainly due to the multiple clouds in the line of sight. A detailed analysis of the large-scale kinematics of the molecular gas could lead to new insights concerning the feedback of massive star formation on its surrounding molecular gas, but this theme seems beyond the scope of this study.

3.2. Distances to Structures

Since the distance for each velocity component is only slightly different over a 10 degree longitude range, for simplicity we adopt a constant distance to estimate the parameters for each velocity component. Distances for the Local and Perseus arms were reviewed by Straižys & Laugalys (2008) and Megeath et al. (2008), respectively. The distance of the Gould Belt substructure in this region is about 160–260 pc (e.g., Fich & Blitz 1984; Turner & Evans 1984), and the

Table 2
Statistics of Excitation Temperatures

Layer Name	Mask Region	Min. (K)	Max. (K)	Median (K)	Mean (K)	S.D. (K)	Percentage $T_{ex} \leqslant 7.5$
Local	B	3.5	21.0	6.3	6.7	1.57	74.2%
	G	4.6	21.0	9.0	9.1	1.66	17.4%
	R	9.4	20.1	11.0	12.4	3.34	0 %
Interarm1	B	3.5	19.4	6.0	6.6	2.05	76.6%
	G	5.5	19.4	10.5	10.9	2.66	6.9%
Perseus	B	3.7	54.3	6.6	7.8	3.55	63.1%
	G	4.2	54.3	11.5	12.2	4.27	7.5%
	R	9.9	54.3	18.7	20.3	6.98	0%
Interarm2	B	3.6	10.5	5.5	5.8	1.03	92.7%
	G	6.3	9.9	7.8	8.0	0.88	28.8%
Outer	B	4.1	15.3	5.5	5.8	1.08	94.5%
	G	5.4	15.3	7.8	8.6	2.15	44.4%
OSC	B	4.3	9.2	5.3	5.6	0.98	94.3%
	G	5.7	9.2	8.5	8.2	1.03	21.4%

Note. Refer to Table 1 for the pixel number of each region. The last column is the pixel percentage for each mask region, which has an excitation temperature $\leqslant$7.5 K.

Cam OB 1 substructure is about 1 kpc away from us (e.g., Humphreys 1978; Straižys & Laugalys 2007). The two substructures are generally within the intrinsic widths of a spiral arm, which has a typical value of several hundred parsecs. Hence, they may represent the inner and outer regions of the Local arm, so we adopt a middle value of 600 pc for the Local arm in this study. This value is also consistent with the kinematic distance derived from the median velocity $V_{lsr} \sim -11$ km s^{-1} of the Local arm on the assumption of the Reid rotation curve.

In the Perseus arm, parallax distances of 1.95 kpc and 2.4 kpc were measured toward the high-mass star-forming region W3(OH) at $l = 133.^{\circ}94$, $b = 1.^{\circ}06$ (Xu et al. 2006) and the evolved star SPer at $l = 134.^{\circ}62$, $b = -2.^{\circ}19$ (Asaki et al. 2010). Since the dense part of the molecular gas arm is well correlated with W3(OH), while no CO emission is detected around SPer, we adopt the former distance as the distance to the Perseus arm. In the Outer arm, trigonometric parallax measurements of the star-forming region WB 89–437 at $l = 135.^{\circ}27$, $b = 2.^{\circ}79$ give a distance of 5.99 kpc (Reid et al. 2014), which is adopted by this study. We note that the kinematic distances of the Perseus and Outer arms are both overestimated. The Perseus arm exhibits a mean V_{lsr} departure of ~ -16 km s^{-1} in this Galactic range, which is consistent with previous studies (e.g., Brand & Blitz 1993). In addition, we obtain a mean V_{lsr} departure of ~ -9 km s^{-1} in the Outer arm in the G130 region. This negative value is obviously different from the results of Russeil et al. (2007), who reported a positive departure in the second Galactic quadrant using the photometric distance of H II regions. Since the distances from VLBI parallax observations are of better accuracy, we suggest that our results may represent a more reliable V_{lsr} departure of the Outer arm in this Galactic range.

In the OSC arm, the photometric distance of one cluster at $l = 131.^{\circ}0$, $b = 1.^{\circ}5$ was estimated to be greater than 12 kpc (Izumi et al. 2014). The kinematic distances derived from the radial velocities of CO emission from the OSC arm are in the range of 10–15 kpc, assuming the Reid rotation curve. Therefore, we finally adopt a value of 13 kpc as the distance to the OSC arm. Distances of 1.28 and 3.98 kpc for the two inter-arms can be derived by assuming that the inter-arms have equal distances to the adjacent spiral arms.

3.3. Derivation of Column Densities

The column density can be derived from ^{12}CO by adopting a CO-to-H_2 X conversion factor ($X_{co} \equiv N_{H_2}/I_{CO}$) from ^{13}CO and C^{18}O by assuming local thermodynamic equilibrium (LTE) and abundance ratios of H_2 to ^{13}CO and C^{18}O, hereafter the X-factor method and LTE method. Applying the LTE method to an optically thin tracer (e.g., the commonly used ^{13}CO and C^{18}O) is thought to be one of the most direct approaches to estimating the H_2 column density (Bolatto et al. 2013).

3.3.1. Column Densities from ^{13}CO and C^{18}O Emission

In addition to ^{12}CO, at least one optically thin isotopologue is detected in the mask "G" and "R" regions, and therefore the LTE method is adopted to determine the column density for regions where ^{13}CO and C^{18}O are detected.

We determine the excitation temperature from the peak value of ^{12}CO by assuming that ^{12}CO is optically thick. The excitation temperature T_{ex} of each pixel can be expressed as (e.g., Garden et al. 1991)

$$T_{ex} = \frac{5.5}{\ln(1 + 5.5\ \mathrm{K}/(T_{max}(^{12}\mathrm{CO}) + 0.82)}. \quad (1)$$

The derived excitation temperatures for each structure in the mask regions are summarized in Table 2 and are plotted as histograms in Figure 9. In the mask "B," "G," and "R" regions, the median excitation temperatures are distributed from 5.3 to 6.6 K, from 7.8 to 11.5 K, and from 11 to 18.7 K, while the mean excitation temperatures are distributed from 5.6 to 7.8 K, from 8.0 to 12.2 K, and from 12.4 to 20.3 K for different velocity structures, respectively. Being collisionally excited, the excitation temperature of ^{12}CO is expected to show the

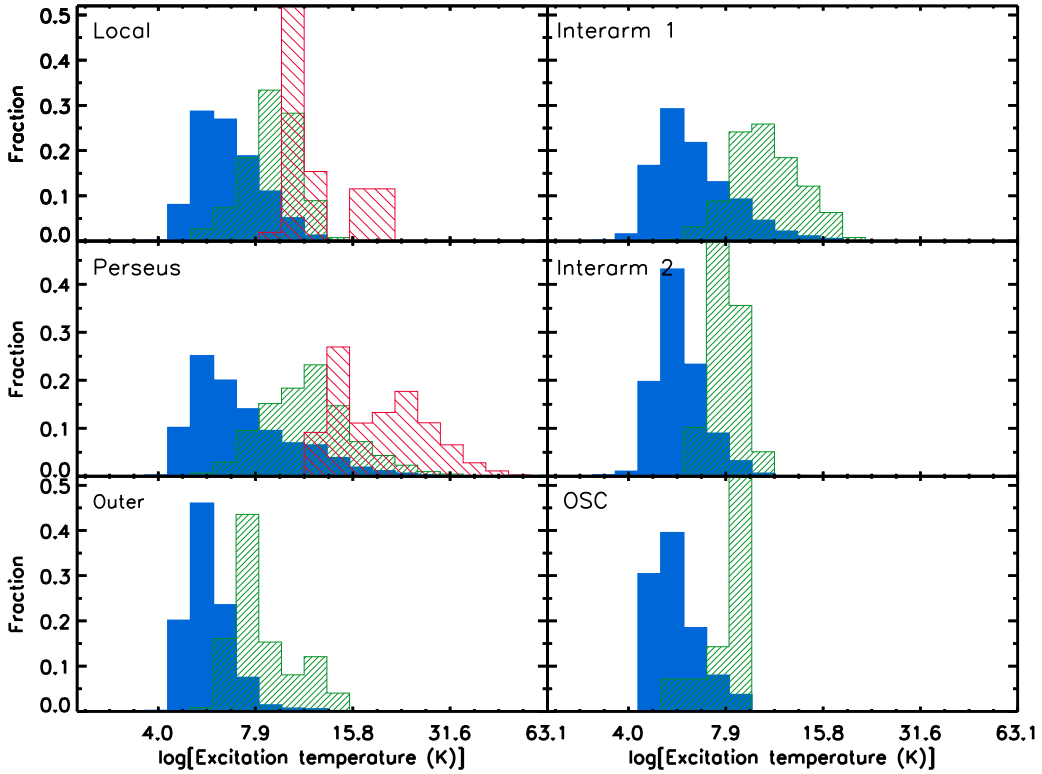

Figure 9. Histograms of excitation temperatures of each structure. The distributions of T_{ex} in the mask "B" region are shown in blue, in the mask "G" region by green, and in the mask "R" region by red. The total pixel numbers in each mask region are listed in Table 1.

lowest value in region "B," the outskirts of the cloud, and to show the highest value in region "R," the densest part of the cloud.

Following Goldsmith et al. (2008), the last column of Table 2 gives the pixel percentage that has an excitation temperature of $\leqslant$7.5 K. The results reveal that more than 60% of the observed ^{12}CO emission has excitation temperatures $\leqslant$7.5 K, which are similar to those found in Taurus and Perseus (Goldsmith et al. 2008; Pineda et al. 2008). Note that we assume a uniform unity filling factor for all velocity structures with different distances. Therefore, as expected, the pixel percentages increase up to ~90% in the outer or extremely outer regions, where smaller beam filling factors are expected at larger distances than the more nearby regions. A large fraction of the areas present excitation temperatures lower than the typical kinetic temperatures of molecular clouds (~10 K). This is likely because the volume density of the gas is lower than the critical density of ^{12}CO or the filling factor of ^{12}CO emission is lower than unity, as suggested by Heyer et al. (2009).

We assume that different isotopologues have the same T_{ex}. Then the optical depths τ of ^{13}CO and C^{18}O can be derived by

$$\tau(^{13}\mathrm{CO}) = -\ln\left(1 - \frac{T_{\max}(^{13}\mathrm{CO})/5.29}{1/(e^{5.29/T_{ex}} - 1) - 0.16}\right) \quad (2)$$

and

$$\tau(\mathrm{C}^{18}\mathrm{O}) = -\ln\left(1 - \frac{T_{\max}(\mathrm{C}^{18}\mathrm{O})/5.27}{1/(e^{5.27/T_{ex}} - 1) - 0.17}\right). \quad (3)$$

The obtained optical depths of ^{13}CO and C^{18}O are used to make saturation corrections to the ^{13}CO and C^{18}O column densities derived by assuming optically thin emission (e.g., Bourke et al. 1997):

$$N_{^{13}\mathrm{CO}} = 2.42 \times 10^{14} \frac{T_{ex+0.88}}{1 - e^{-5.29/T_{ex}}} \int \tau_{^{13}\mathrm{CO}} dv \quad (4)$$

and

$$N_{\mathrm{C}^{18}\mathrm{O}} = 2.54 \times 10^{14} \frac{T_{ex+0.88}}{1 - e^{-5.27/T_{ex}}} \int \tau_{\mathrm{C}^{18}\mathrm{O}} dv. \quad (5)$$

Isotopic ratios $[^{12}\mathrm{C}/^{13}\mathrm{C}] = 6.2R_{gal}+18.7$ (Milam et al. 2005) and $[^{16}\mathrm{O}/^{18}\mathrm{O}] = 560$ (Wilson & Rood 1994) are used to convert the ^{13}CO and C^{18}O column density into the ^{12}CO column density. We then derive the H_2 column density with a constant $[H_2/^{12}\mathrm{CO}]$ abundance ratio of 1.1×10^4 (Frerking et al. 1982). Here we should point out that the ^{12}CO abundance with respect to H_2 is likely to vary, with an order of magnitude scatter (e.g., Sheffer et al. 2008). A lower CO abundance is expected for the more distant structures based on metallicity gradients. This means the actual H_2 column densities could rise slightly as we go farther out in the Galactic disk.

In the mask "R" region where both ^{13}CO and C^{18}O emission is detected, the H_2 column densities derived by these two isotopologues are not exactly the same. The discrepancy might be explained by the abundance variations of these isotopologues across different environments. Because of different levels of the self-shielding effect (e.g., van Dishoeck & Black 1988; Shimajiri et al. 2015), C^{18}O is selectively dissociated by far-ultraviolet (FUV) emission more effectively than is ^{13}CO. Detailed analyses of the ^{13}CO and C^{18}O abundance variations have been done for MWISP data in other Galactic longitude

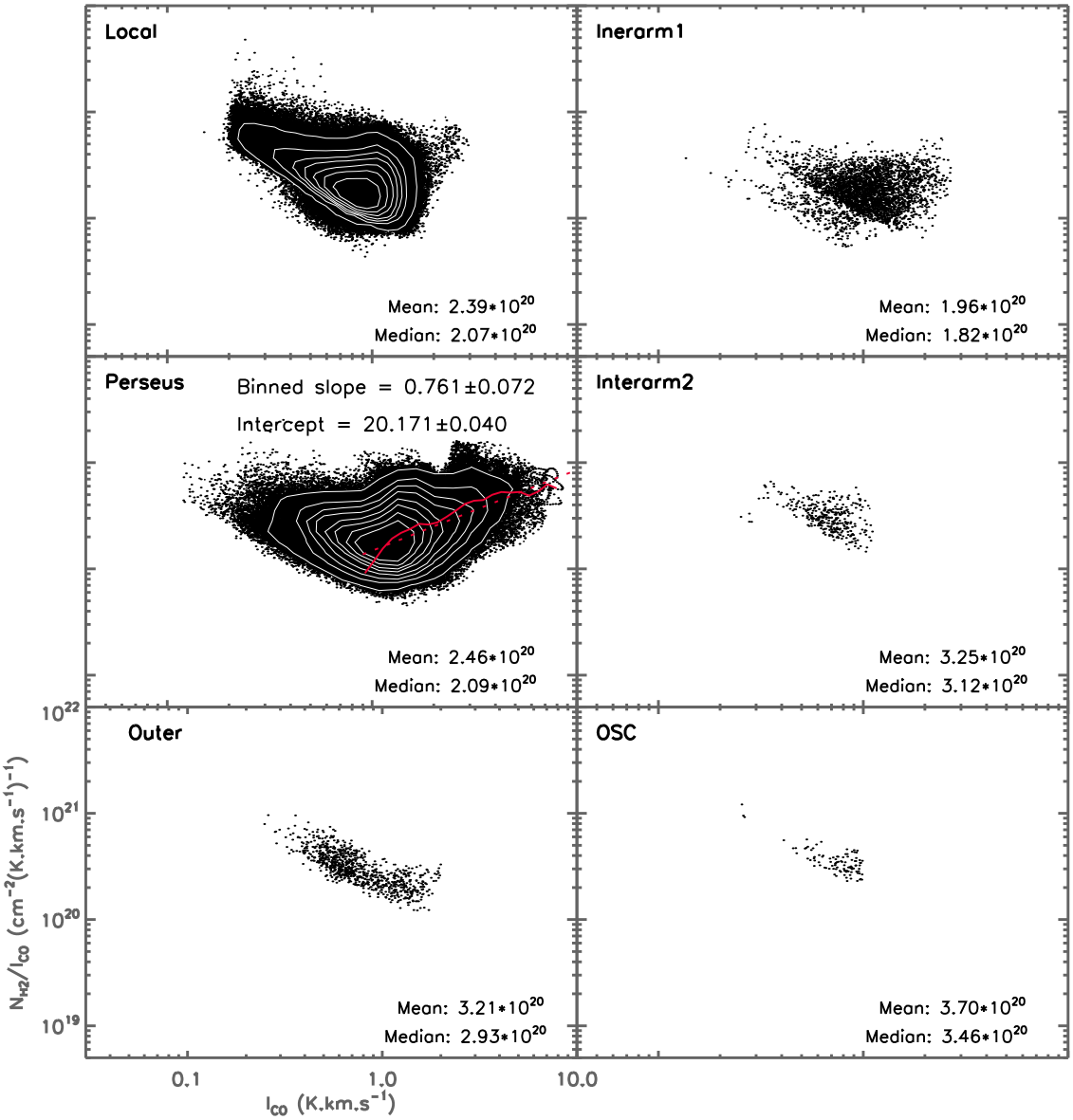

Figure 10. Relations between N_{H_2}/I_{CO} and I_{CO} for each structure. Each black point represents a voxel with a channel width of 0.168 km s^{-1} that shows both ^{13}CO and ^{12}CO detections. The white contours show the surface density of points. The points with $I_{CO} > 0.8$ K km s^{-1} are binned in log(I_{CO}). The mean values of N_{H_2}/I_{CO} of each bin are computed and indicated by the red solid line, and the red dashed line is a least-squares fit to the binned data.

ranges (Wang et al. 2019). Similar analyses of current data will be presented in a future paper.

3.3.2. Column Densities from ^{12}CO Emission

In the mask "B" region where ^{12}CO emission is detected, the column density is determined by the X-factor method. Recent theoretical/numerical (e.g., Feldmann et al. 2012; Gong et al. 2018) and observational (e.g., Barnes et al. 2015; Kong et al. 2015; Barnes et al. 2018) studies have suggested an X factor that varies significantly with several effects (e.g., excitation, abundance, opacity, and resolution). Besides, the X factor was found to increase with decreasing metal abundance (Bolatto et al. 2013). Since the ^{12}CO emission in each structure may have very different conditions, a constant conversion factor may not be applicable to each and every structure. Similar to the work of Barnes et al. (2018), we derive the X_{CO} factor from these pixels where both ^{12}CO and ^{13}CO are detected in each velocity structure. Figure 10 shows the relations between N_{H_2}/I_{CO} and I_{CO}. Each black point in Figure 10 represents a voxel with a channel width of 0.168 km s^{-1} that shows both ^{12}CO and ^{13}CO detections. Our results confirm that the N_{H_2}/I_{CO}–I_{CO} relation shows a negative slope at low I_{CO} and a positive slope at high I_{CO}, although the slope varies somewhat from region to region. A least-squares fit is only applied for the Perseus arm. The mean and median values of X_{co} for each velocity structure are indicated in each panel, which seem to confirm the increase in X_{CO} with decreasing metallicity. If considering the variation of CO abundance with location (see Section 3.3.1), the X conversion factors would be shifted to even higher values for the more distant structures.

Similar to Figure 9 of Barnes et al. (2018), in Figure 11 each quantity is integrated across all velocity channels with detectable ^{12}CO emission, regardless of whether N_{H_2} is defined. As discussed by Barnes et al. (2018), the unmasked versions of the N_{H_2}/I_{CO}–I_{CO} relation (Figure 11) represent the practical conversion laws. However, we suggest that the

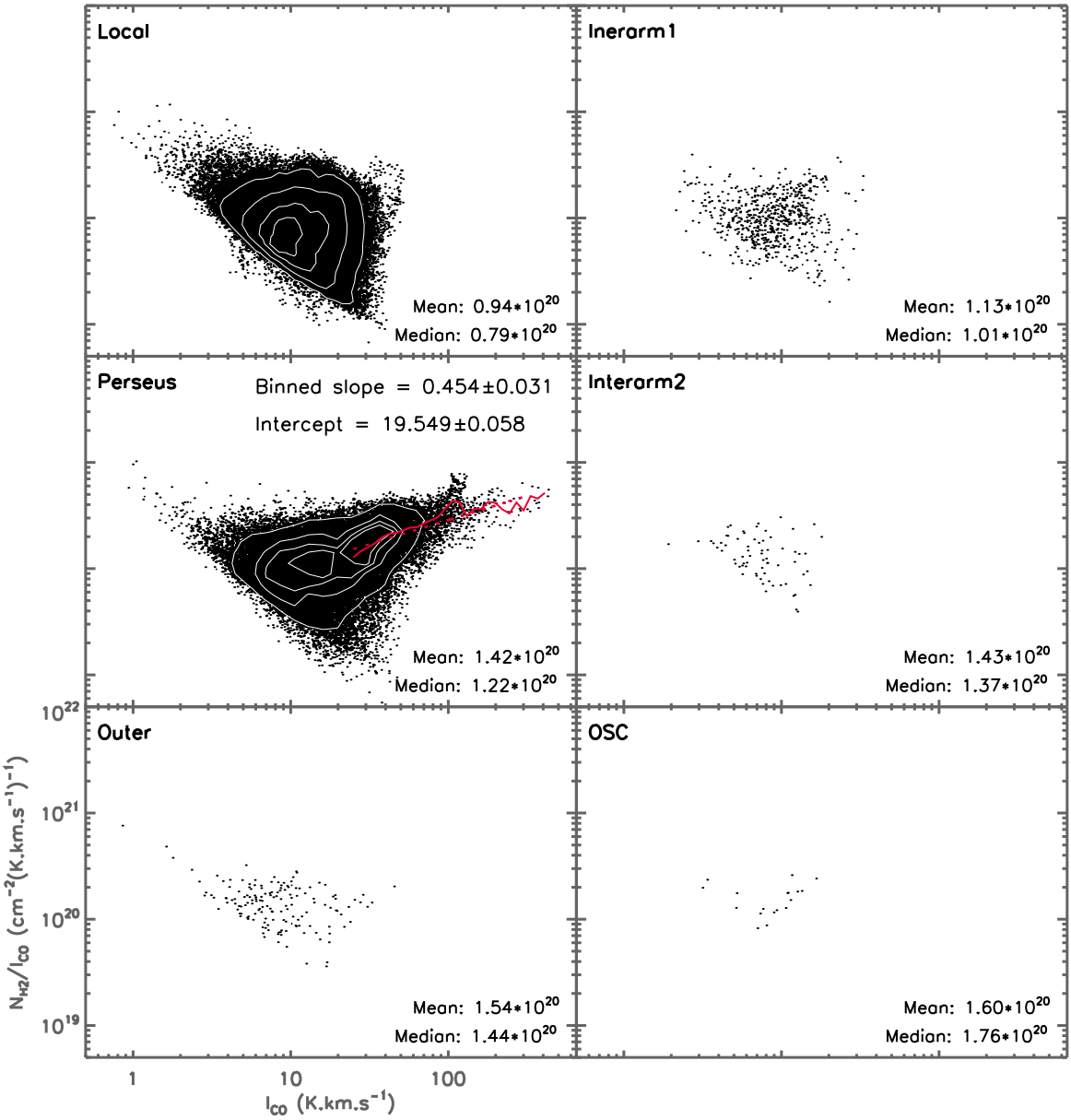

Figure 11. N_{H_2}/I_{CO}–I_{CO} relations as in Figure 10, but each quantity is integrated over all velocity channels with detectable ^{12}CO emission, regardless of whether N_{H_2} is defined.

derived X_{CO} conversion factors in Figure 11 represent lower limits. Because of the large velocity coverage for each structure (up to ~30 km s^{-1}, see Table 1), any small nonrelevant components will enhance the I_{CO} and then lower the X_{CO}. This means that the practical X_{CO} conversion factor might fall in a range between the values listed in Figure 10 and Figure 11. Therefore, we adopt mean values of $X_{co} = 1.59 \times 10^{20}$, 1.55×10^{20}, 1.94×10^{20}, 2.34×10^{20}, 2.37×10^{20}, and 2.65×10^{20} cm^{-2}(K km s^{-1})$^{-1}$ for the Local arm, Interarm1, Perseus arm, Interarm2, Outer arm, and OSC arm, respectively.

Table 3 gives a summary of the basic statistical parameters of the obtained H_2 column densities of each velocity structure from different methods (LTE and X-factor methods) and different molecular lines (^{12}CO, ^{13}CO, and C^{18}O), including the mean and median values and the standard deviations. Figure 12 shows the distributions of the H_2 column densities, plotted as histograms for each structure in mask "B" (blue), "G" (green), and "R" (red) regions. Note that the H_2 column densities for the mask "G" and "R" regions are translated from ^{13}CO and C^{18}O, respectively. It is evident that mask "B," "G," and "R" regions encompass the relatively low, modest, and high column density gas, which is presumably characterized by low, modest, and high volume density, respectively. We also see that in most velocity structures, the column density probability density functions (PDFs) show an approximate lognormal shape at low column density. However, in the Perseus arm, significant departures from lognormal distributions are found at the higher column density tail. The departure from lognormal form has been interpreted as an indicator of the formation of dense, gravitationally bound structures inside more diffuse, large-scale molecular clouds, and that is the ultimate prerequisite for star formation (e.g., Kainulainen et al. 2010; Lombardi et al. 2010; Brunt 2015). These results may suggest that the Perseus arm shows more active star formation

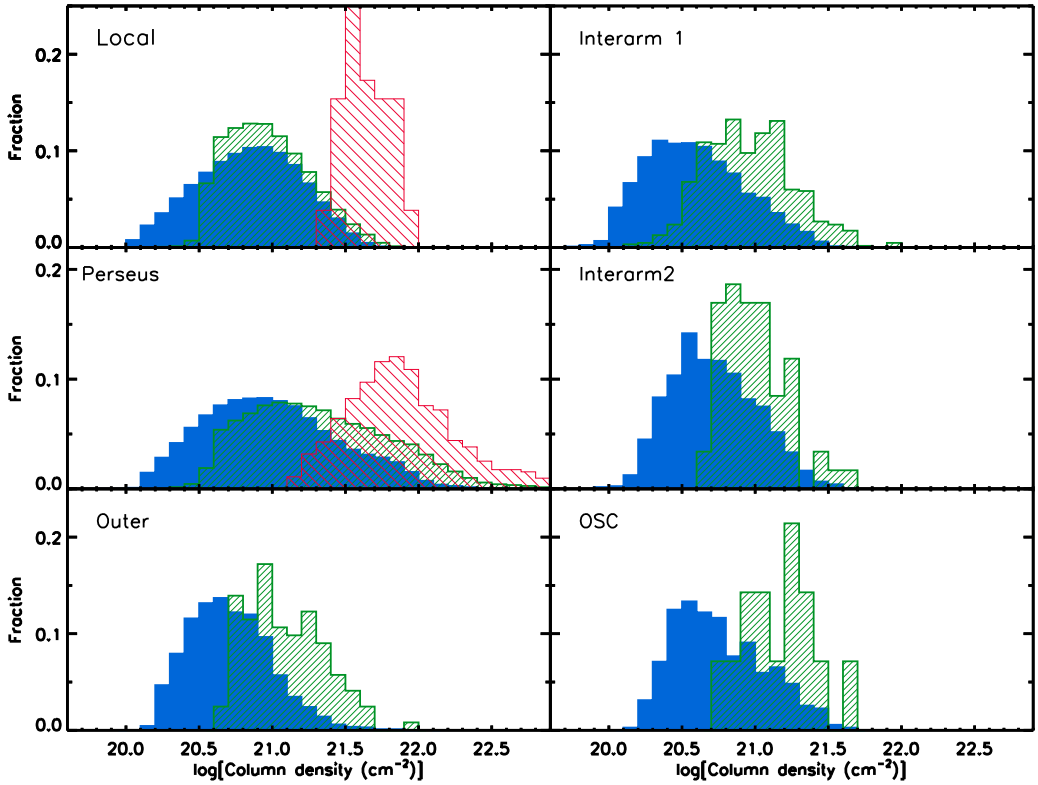

Figure 12. Histograms of H_2 column density distributions of each structure. H_2 column densities are derived from ^{12}CO, ^{13}CO, and C^{18}O for the mask "B," "G," and "R" regions, respectively. The color code is the same as in Figure 9.

Table 3
Statistics of log[N_{H_2}], Mass, and Surface Density

Layer Name	Mask Region	log[N_{H_2}] Min.	Max.	Median (cm^{-2})	Mean	S.D.	Mass ($M_\odot$)	Σ_{gas} ($M_\odot$ pc^{-2})
Local	B	19.7	21.9	20.9	20.8	0.35	9.1(4)	21.0
	G	20.1	22.2	20.9	21.0	0.28	1.4(4)	25.1
	R	21.4	21.9	21.6	21.6	0.15	6.0(1)	89.0
Interarm1	B	19.6	21.7	20.6	20.6	0.33	3.1(3)	12.0
	G	20.2	21.9	20.9	21.0	0.30	5.8(2)	24.7
Perseus	B	19.9	22.9	21.0	21.0	0.45	4.1(5)	40.2
	G	20.2	23.4	21.3	21.3	0.48	2.5(5)	92.9
	R	21.1	23.2	21.8	21.9	0.38	3.4(4)	248.2
Interarm2	B	19.9	21.6	20.7	20.7	0.29	5.9(3)	14.8
	G	20.7	21.6	21.0	21.0	0.22	5.5(2)	23.8
Outer	B	20.0	22.0	20.7	20.7	0.28	4.0(4)	14.5
	G	20.6	22.0	21.1	21.1	0.27	3.6(3)	30.4
OSC	B	20.2	21.6	20.7	20.8	0.31	2.1(4)	16.9
	G	20.8	21.6	21.2	21.2	0.25	2.1(3)	33.4

Note. Refer to Table 1 for the pixel number of each region. The number in parentheses is the order of magnitude of the gas mass.

activity. The star formation activities in different velocity structures are investigated in detail in Section 4.

3.4. Masses and Surface Densities

The mass of each structure is estimated by integrating the column density over the area of each mask region. The molecular gas surface density, Σ, of each structure is simply the H_2 mass divided by the projected area, $\Sigma = M/(\pi\ r^2)$. The estimated total mass and surface density of each structure are also listed in Table 3. We should note that the detection limits of the gas mass for each structure along the line of sight are quite different and are about 0.1, 0.4, 0.8, 7.7, and 36.1 $M_\odot$ for the Local arm, Interarm1 region, Perseus arm, Interarm2

region, Outer arm, and OSC arm (for 3σ and narrow emission only encompassing three channels and three pixels in the l–b space), respectively. Since a large fraction of the molecular gas is found to be located in regions with low excitation conditions (refer to Section 3.3), the amount of underestimated gas will increase with increasing distance.

The molecular gas masses traced by ^{12}CO, ^{13}CO, and C^{18}O across different structures are distributed from 3.1×10^3 to 4.1×10^5 $M_\odot$, from 5.5×10^2 to 2.5×10^5 $M_\odot$, and from 60 to 3.4×10^4 $M_\odot$, respectively. The total molecular gas masses of the entire mapped area (all spiral arms and inter-arm regions) traced by ^{12}CO, ^{13}CO, and C^{18}O are estimated to be 5.7×10^5, 2.7×10^5, and 3.4×10^4 $M_\odot$, respectively. We find that the mass is not uniformly distributed in different structures, with a mass difference of an individual structure as high as two orders of magnitude. The majority of the molecular gas masses (∼90%) are located in the two more nearby arms, the Perseus arm (∼70%) and the Local arm (∼20%). Even though it is considered that their masses might have been underestimated, the two distant spiral arms contribute a small portion of the total molecular gas mass (∼10%). We see that the molecular gas masses drop dramatically beyond the Perseus arm. Our results also support the suggestion that the Perseus arm is one of the dominant spiral arms, which has been known for some time (e.g., Georgelin & Georgelin 1976; Yang et al. 2002).

We further estimate the arm-to-inter-arm contrast in total molecular gas mass by dividing the mass between the adjacent spiral arm and inter-arm. The mass contrasts of Local-to-Interarm1, Perseus-to-Interarm1, Perseus-to-Interarm2, and Outer-to-Interarm2 are 29, 132, 69, and 7 as traced by ^{12}CO emission, and are 24, 431, 455, and 7 as traced by ^{13}CO emission. When averaged over all spiral arms and inter-arms, the arm-to-inter-arm mass contrasts are 62 and 239 as traced by ^{12}CO and ^{13}CO emission, respectively. This indicates that the mass contributions from the two inter-arm regions are negligible. In other words, the molecular gas components, especially the dense molecular gas components, are generally confined to spiral arms. Therefore, we suggest that the ^{13}CO and C^{18}O molecular lines are better arm tracers than the ^{12}CO molecular line for the nearby spiral arms.

The derived surface gas densities range from 12 to 40 $M_\odot$ pc^{-2}, 24 to 93 $M_\odot$ pc^{-2}, and 89 to 248 $M_\odot$ pc^{-2} in the mask "B," "G," and "R" regions of different velocity structures. As expected, the surface gas densities increase as we move from region "B," the outskirts of MCs, which contains a significant amount of diffuse gas, to the denser regions "G" or "R," which are dominated by high-column-density gas. In addition, the surface gas densities in the Outer and OSC arms are much smaller than in the Perseus and Local arms. This suggests the decrease of the surface gas density with the increase of Galactic radii, which is in agreement with the findings reported in other Galactic longitude ranges (Heyer & Dame 2015).

3.5. Area Ratios and Mass Ratios

Many studies have suggested that it is primarily the dense gas component, not the diffuse gas component, of a molecular cloud that actively participates in star formation (e.g., Gao & Solomon 2004a, 2004b; Wu et al. 2005, 2010; Lada et al. 2010). Therefore, it is essential to understand approximately how much gas is in the dense phase. Although the typical densities traced by ^{13}CO and C^{18}O (∼10^3–10^4 cm^{-3}) are not as high as those of the commonly used dense gas tracers (e.g., CS, HCN, and N_2H^+), they do trace relatively higher density regions of the molecular clouds than ^{12}CO, as mentioned in Section 1. Using ^{12}CO, ^{13}CO, and C^{18}O emission, Torii et al. (2019) approximately examined the dense gas fraction (f_{DG}) in the first Galactic quadrant and found that f_{DG} in the Galactic arms (averaged over all spiral arms along the line of sight) is much higher than in the Galactic bar and inter-arm regions. Given the fact that star formation primarily takes place in the spiral arm, it is reasonable to expect such a trend.

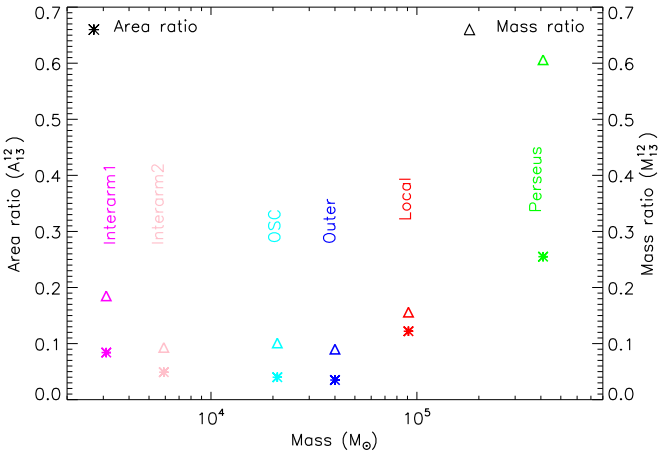

Figure 13. The area ratio (A_{13}^{12}) and mass ratio (M_{13}^{12}) of each structure are indicated by stars and triangles, respectively.

Table 4
Area and Mass Ratios

Layer Name	A_{13}^{12} (%)	M_{13}^{12} (%)	A_{18}^{12} (%)	M_{18}^{12} (%)
Local	12.2	15.6	0.01	0.07
Interarm1	8.4	18.5	…	…
Perseus	25.5	60.6	1.2	8.2
Interarm2	4.9	9.3	…	…
Outer	3.5	9.0	…	…
OSC	4.0	10.1	…	…

Note. Refer to Section 3.5 for definitions of the area and mass ratios.

Attempting to obtain such a view, we define area and mass ratios by quantifying the area and mass traced by ^{12}CO, ^{13}CO, and C^{18}O in this section (see Table 4). To a certain extent, these ratios traced by the different isotopologues may offer valuable insights into the spatial and mass distributions of the molecular gas. The area ratios A_{13}^{12} and A_{18}^{12} are defined as ratios of $A(^{13}\mathrm{CO})$ to $A(^{12}\mathrm{CO})$ and $A(\mathrm{C}^{18}\mathrm{O})$ to $A(^{12}\mathrm{CO})$, where $A(^{12}\mathrm{CO})$, $A(^{13}\mathrm{CO})$, and $A(\mathrm{C}^{18}\mathrm{O})$ are the areas with detectable ^{12}CO (mask "B"), ^{13}CO (mask "G"), and C^{18}O (mask "R") emission, respectively. Similarly, the mass ratios M_{13}^{12} and M_{18}^{12} are defined as ratios of $M(^{13}\mathrm{CO})$ to $M(^{12}\mathrm{CO})$ and $M(\mathrm{C}^{18}\mathrm{O})$ to $M(^{12}\mathrm{CO})$, where $M(^{12}\mathrm{CO})$, $M(^{13}\mathrm{CO})$, and $M(\mathrm{C}^{18}\mathrm{O})$ are the total masses contained in the areas $A(^{12}\mathrm{CO})$, $A(^{13}\mathrm{CO})$, and $A(\mathrm{C}^{18}\mathrm{O})$, respectively. These ratios are summarized in Table 4.

In Figure 13, the area ratios and the mass ratios are plotted as a function of the total mass of each structure. Obviously, neither area ratios nor mass ratios seem to be related to the total mass of each structure. The derived area ratios A_{13}^{12} and A_{18}^{12} are in the range of 4%–26% and 0.01%–1% in different velocity structures, respectively. It seems that a small or negligible fraction of the cloud area exhibits detectable ^{13}CO or

$C^{18}O$ emission. The derived mass ratios M_{13}^{12} and M_{18}^{12} have slightly larger values than the area ratios and are in the range of 9%–61% and 0.07%–8% in different velocity structures, respectively. We see that the contributions from the relatively dense molecular gas traced by ^{13}CO or $C^{18}O$ are very small or negligible. In other words, a large fraction of the area and mass is in relatively low-density gas. The only exception is the Perseus arm, in which about one-half of the total mass is in the relatively dense phase and is concentrated within about one-fourth of the total mask area we have studied.

We can also see that the Perseus arm has much higher values of area ratio A_{13}^{12} and mass ratio M_{13}^{12} than the inter-arm regions, while the ratios in the Local, Outer, and OSC arms show no significant differences from those in the two inter-arm regions. One possible explanation is that, unlike the Perseus arm, these spiral arms are not the dominant spiral arms in this Galactic range. Future statistics over a wider Galactic longitude range will give a more representative value. Moreover, we find if we average over all spiral arms and inter-arm regions along the line of sight, these ratios have higher values in the spiral arms than in the inter-arm regions, which is similar to the finding in the first Galactic quadrant by Torii et al. (2019).

4. Current High-mass Star Formation

Comparative studies of the physical properties of molecular gas and the relation of these properties to the star formation activities within them may offer significant clues regarding the physical origin of the different levels of star formation activity in molecular gas (Lada et al. 2010). The ∼100 deg^2 ^{12}CO, ^{13}CO, and $C^{18}O$ data presented in this study cover a wide range of physical environments and thus afford an opportunity to extend these comparative studies.

We systematically examine in this section the spatial distribution of the current high-mass star formation sites with respect to the molecular gas. H II regions, the 22.2 GHz water masers, and the 6.7 GHz methanol masers are among the most readily observed signposts of massive star formation. In particular, the H II regions and the 6.7 GHz methanol masers, due to their short lifetimes, are clear indicators of ongoing massive star formation and are therefore good tracers of Galactic spiral structure (Hou et al. 2009). Over the past few decades, extensive searches of masers and H II regions have provided a wealth of catalogs of massive star formation regions in our Galaxy. To date, more than 1000 massive star-forming regions in our Galaxy have been reported by the presence of interstellar maser emission, mainly from transitions of methanol (e.g., Pestalozzi et al. 2005; Xu et al. 2008; Sun et al. 2014; Green et al. 2017; Sun et al. 2018) and water (e.g., Comoretto et al. 1990; Valdettaro et al. 2001; Szymczak et al. 2005; Breen et al. 2007; Urquhart et al. 2009; Caswell & Breen 2010; Walsh et al. 2011; Titmarsh et al. 2014; Xi et al. 2015, 2016; Titmarsh et al. 2016). Besides, there are about 3000 Galactic H II regions from the catalog compiled by Hou & Han (2014) along with the later radio recombination line (RRL) or radio continuum surveys of the Galactic H II region (Anderson et al. 2014, 2015; Foster & Brunt 2015).

We conduct a survey of the literature and the SIMBAD database and compile a list of high-mass star-forming sites within the Galactic range of this study. The search results in a total of 19 interstellar masers and 32 H II regions in this exact G130 region. In Table 5, we list the positions of the masers along with the corresponding references and Gaussian fitting results of the associated ^{12}CO, ^{13}CO, and $C^{18}O$ emission from our new observations. Note that when multiple velocity components are detected along the line of sight, only the fitting results for the associated components are presented. One sigma noise level is given for those isotopologues without clear detections. Three regions marked with "*" are associated with both the 22.2 GHz water and the 6.7 GHz methanol masers, the remaining regions being only associated with water masers. We assign masers to each velocity structure based on association with the structure seen in longitude–velocity plots of ^{12}CO and its isotopologues. Interestingly, masers seem to be exclusively associated with the Perseus arm, except for two masers that are associated with the Outer arm and Interarm1. We further examine the positional relationship between the molecular gas distribution and the masers in the $l-b$ space to investigate the reliability of the associations (Figures 6–8). We see that all masers are distributed in the densest portion of the molecular gas, which confirms the associations.

Similarly, the results for the 32 H II regions are summarized in Table 6. The LSR velocity of the H II regions (Column 3) direct from the literature were measured from RRL (marked with "*R*" in Column 4), CS (marked with "*C*" in Column 4), CO, or H_α emission. We find that no CO emission is detected by our new data toward four of 32 H II regions (those sources marked with "⋆" in Table 6) with typical rms noise level of 0.5 K, but once we consider the size of the H II region, those four H II regions all have a CO counterpart. Toward the remaining 28/32 regions, at least one CO isotopologue is detected. The LSR velocities of the 25/28 H II regions and the CO emission are in agreement with each other with offset less than 5 $km\,s^{-1}$. The velocity differences are larger than 20 $km\,s^{-1}$ for three of 28 H II regions (marked with "†" in Table 6), which makes spiral arm assignments challenging. All detected velocity components in CO emission are tabulated for those three H II regions. Finally, 2, 24, 2, and 1 H II regions are assigned to the Local, Perseus, Outer, and OSC arms based on the *l*–*b*–*v* information. Their spatial distributions with respect to the molecular gas reveal that those 16 H II regions with measured RRL or CS(2–1) dense gas emission (indicated by white plus) are restricted to the densest portion of the molecular gas, and therefore are often associated with interstellar maser emission. The remaining H II regions (indicated by red pluses) are located in regions with relatively weak CO emission. We note that the majority of those H II regions are identified by optical H_α emission, so part of the molecular gas has likely been dispersed by the winds from the newly formed stars.

Here we should note that the current interstellar maser catalogs of this region are from targeted surveys mainly toward IRAS or *WISE* selected point sources, rather than from unbiased blind surveys. In addition, a portion of the faint H II regions or masers may be missed. Therefore, in the future, new observations may find some more new H II regions and interstellar masers, in other words more massive star-forming regions. However, it will not likely change the current trend that significant variations exist in massive star formation activity among different velocity structures along the line of sight. High-mass star formation in the Perseus arm is prominent, and it is negligible in the other spiral arms and inter-arm regions. A census of ongoing both low- and high-mass star-forming sites traced by CO outflow across the whole mapped area also revealed a similar trend. The number of outflow candidates was found to vary considerably across the

Table 5
22.2 GHz Water Masers and 6.7 GHz Methanol Masers

				CO			^{13}CO			C^{18}O			
	l	b	References	$V_{\rm lsr}$	$T_{\rm Peak}$	I	$V_{\rm lsr}$	$T_{\rm Peak}$	I	$V_{\rm lsr}$	$T_{\rm Peak}$	I	Spiral
	(°)	(°)		(km s^{-1})	(K)	(K km s^{-1})	(km s^{-1})	(K)	(K km s^{-1})	(km s^{-1})	(K)	(K km s^{-1})	Arm
(1)	(2)	(3)	(4)	(5)	(6)	(7)	(8)	(9)	(10)	(11)	(12)	(13)	(14)
1	132.157	−0.726	2	−54.9	11.5	55.2	−55.1	3.5	10.3	−54.9	0.6	1.2	Per
2	133.688	+1.224	1	−43.4	45.0	356.8	−43.4	9.4	59.1	−43.7	0.8	4.6	Per
3	133.718	+1.215	1	−41.5	36.7	180.2	−39.0	10.6	64.4	−38.8	1.2	5.7	Per
				−35.6	28.9	178.7		0.09					
4	133.748	+1.059	6	−43.2	20.7	41.0	−43.3	8.4	12.0	−43.2	1.2	1.8	Per
				−40.7	10.6	25.3	−40.8	2.2	3.3		0.27		
5	133.751	+1.198	1	−38.9	26.6	142.1	−39.0	11.3	33.4	−39.0	1.6	4.1	Per
6	133.783	+1.420	2	−42.8	14.0	38.1	−43.2	3.1	4.9		0.19		Per
				−38.6	5.0	6.3		0.23			…		
7*	133.951	+1.065	1, 4	−47.6	27.1	212.7	−47.4	12.4	61.8	−47.3	1.5	6.8	Per
8	134.207	+0.729	8	−48.5	18.5	129.1	−48.4	11.8	46.1	−48.6	4.0	8.3	Per
9	134.279	+0.856	3	−51.4	15.5	51.7	−51.4	5.8	11.4	−51.2	0.7	0.8	Per
10	134.831	+1.312	1	−40.0	9.2	29.0	−39.8	3.8	8.3	−39.6	0.7	1.1	Per
11	135.282	+2.796	1	−72.0	7.7	31.1	−71.9	1.8	5.2		0.32		Out
12	135.894	−0.459	1	−26.2	14.0	27.8	−26.4	2.9	4.4		0.26		Int
13	136.387	+2.269	1	−42.2	15.0	61.5	−42.3	3.3	9.9		0.27		Per
14*	136.846	1.149	3, 4	−42.0	20.4	86.3	−42.7	9.5	25.1	−42.8	1.5	2.8	Per
				−36.9	8.5	23.1	−36.6	4.1	3.7		0.30		
15	136.945	+1.092	6	−41.0	18.4	68.0	−41.1	10.2	23.8	−41.1	1.5	3.4	Per
				−35.6	9.1	22.9		0.29			0.29		
16*	137.070	+3.002	1, 5, 7	−51.8	6.7	33.2	−52.0	2.7	6.3		0.21		Per
17	138.297	+1.556	2	−38.0	32.7	159.2	−38.2	12.0	31.4	−38.1	1.2	3.1	Per
18	138.503	+1.644	1	−38.4	18.8	66.5	−38.2	4.4	12.5		0.25		Per
19	139.914	+0.200	1	−39.8	32.1	168.0	−39.9	10.5	33.3	−40.0	1.0	3.1	Per

Note. Three masers marked with "*" are associated with both the 22.2 GHz water and 6.7 GHz methanol masers. The remaining sources are only associated with the 22.2 GHz water masers.
References. [1] Comoretto et al. (1990), [2] Brand et al. (1994), [3] Valdettaro et al. (2001), [4] Pestalozzi et al. (2005), [5] Xu et al. (2008), [6] Xi et al. (2016), [7] Yang et al. (2017), [8] Nakano et al. (2017).

Table 6
H II Regions

					CO			^{13}CO			C^{18}O			
	l	b	V_{lsr}	References	V_{lsr}	T_{Peak}	I	V_{lsr}	T_{Peak}	I	V_{lsr}	T_{Peak}	I	Spiral
	(°)	(°)	(km s^{-1})		(km s^{-1})	(K)	(K km s^{-1})	(km s^{-1})	(K)	(K km s^{-1})	(km s^{-1})	(K)	(K km s^{-1})	Arm
(1)	(2)	(3)	(4)	(5)	(6)	(7)	(8)	(9)	(10)	(11)	(12)	(13)	(14)	(15)
1	132.157	−0.725	−56.39	2^R	−54.9	11.5	55.2	−55.1	3.5	10.4	−54.9	0.6	1.1	Per
2	133.411	+0.085	−48.5	4^R	−49.3	5.5	18.3	−49.2	0.7	1.3		0.20		Per
3	133.720	+1.223	−40.68	2^R	−39.7	33.5	270.4	−39.4	8.0	40.0	−39.2	0.7	3.4	Per
4	133.785	+1.423	−49.42	2^R	−42.9	13.2	31.4	−43.3	2.5	4.3		0.21		Per
					−39.3	1.7	14.4		0.22			…		
5	133.960	+1.080	−53.60	2^R	−48.5	26.2	169.2	−48.3	8.6	31.9	−48.0	0.8	2.7	Per
6	134.235	+0.751	−49.0	1,5^R	−48.5	17.7	84.2	−48.8	5.1	17.1	−49.0	0.4	1.4	Per
7	134.340	+3.560	−9.70	2	−0.6	3.5	6.5		0.27			0.26		Loc
8	134.800	+0.940	−43.90	2	−39.8	4.1	10.2		0.24			0.23		Per
9	135.184	+2.698	−71.5	4^R	−71.0	3.2	8.9		0.28			0.26		Out
10	135.278	+2.797	−71.50	2^C	−71.7	11.3	47.1	−71.9	2.1	8.2		0.31		Out
11	135.870	−0.560	−33.70	2	−42	2.6	4.2		0.27			0.26		Per
					−36.6	1.5	3.1		…			…		
12*	136.000	+2.120	−49.60	2		0.45			0.30			0.29		Per
13	136.080	+2.110	−44.70	2	−48.2	1.3	5.1		0.32			0.28		Per
14	136.110	+2.070	−45.70	2	−47.1	6.6	15.2	−47.3	1.3	1.6		0.28		Per
15	136.133	+2.050	−47.6	4^R	−47.5	1.7	4.2		0.28			0.27		Per
					−44.4	2.4	3.0		…			…		
16†	136.360	−0.380	−29.70	2	−55.0	1.7	1.5		0.29			0.27		
					−2.4	2.1	1.7		…			…		
17	136.384	+2.265	−42.40	2^C	−42.2	15.0	62.0	−42.3	3.3	10.0		0.27		Per
18*	136.450	+2.530	−48.10	2		0.52			0.29			0.29		Per
19*	136.490	−0.320	−31.30	2		0.50			0.28			0.27		Per
20	136.837	+1.137	−39.80	2^C	−42.3	13.6	36.9	−42.7	2.2	3.6		0.31		Per
					−37.5	13.5	39.6	−38.3	4.3	9.1		…		
21	136.900	+1.060	−40.65	2^R	−41.7	15.7	34.5	−41.6	3.1	5.2		0.29		Per
					−35.2	9.0	34.0	−35.4	0.6	2.5		…		
22	137.069	+3.003	−51.60	2^C	−51.8	6.7	33.4	−52.0	2.7	6.3		0.20		Per
23*	137.300	+1.000	−39.20	2		0.49			0.26			0.26		Per
24†	137.380	+0.200	−38.20	2	−2.8	3.5	2.0		0.31			0.32		
25	137.770	−0.950	−103.70	2,3	−103.7	4.2	8.0	−103.8	0.7	1.0		0.24		OSC
26	138.090	+4.120	−53.20	2	−53.1	1.2	1.1		0.25			0.24		Per
27	138.297	+1.556	−38.00	2^C	−38.0	32.7	160.0	−38.2	12.0	31.4	−38.1	1.2	3.1	Per
28	138.494	+1.641	−35.47	2^R	−38.5	13.8	52.4	−38.4	2.6	7.7	−37.7	0.8	0.8	Per
29†	139.660	+2.540	−42.69	2,3	−12.2	6.0	17.6	−12.5	1.1	1.7		0.26		
30	139.910	+0.195	−44.8	4^R	−40.1	30.2	146.4	−40.0	10.6	28.4	−39.7	1.0	2.3	Per
31	139.912	+0.200	−39.40	2^C	−39.5	35.6	177.4	−39.6	10.4	34.7	−39.5	1.0	2.6	Per
32	139.990	+2.090	−10.33	3	−14.1	6.3	13.1	−14.1	1.7	2.0		0.26		Loc
					−9.0	13.0	29.5	−9.4	4.4	6.6		…		

Note. Columns 2–5 give the Galactic coordinates, V_{lsr} of each H II region, and the references: [1] Hughes & Viner (1982), [2] Hou & Han (2014), [3] Foster & Brunt (2015), [4] Anderson et al. (2015), [5] Nakano et al. (2017). The V_{lsr} of H II regions marked with "*R*" and "*C*" are determined from RRL and CS(2–1) observations, respectively. Columns 6–14 give the Gaussian fitting results for ^{12}CO, ^{13}CO, and C^{18}O emission. Only the associated velocity components are presented, except for three sources indicated with "†," for which all detected velocity components are presented. Due to the significant velocity difference between these H II regions and the ^{12}CO emission, they could not be confidently assigned to an arm. A few sources marked with "⋆" are not detected in ^{12}CO emission, but if the size of H II regions is considered, there is associated ^{12}CO emission. Column 15 indicates the spiral arm in which it resides: Loc = Local arm, Per = Perseus arm, Out = Outer arm, OSC = Outer Scutum Centaurus arm.

different velocity structures, with ∼62% in the Perseus arm, ∼35% in the Local arm, ∼1% in the Outer arm, and ∼2% in the two inter-arm regions (Li et al. 2019).

Generally, this star formation picture is consistent with the finding in Section 3.3 that the Perseus arm shows an apparent non-lognormal distribution of the column density at the high-column-density wing, yet approximate lognormal shapes are found for other velocity structures. In addition, as revealed in Section 3.5, the total mass of molecular gas is not significantly different between the Perseus arm and the Local arm, but a much higher fraction of denser gas is found in the Perseus arm than in the Local arm. Therefore, our results may lend support to the view that it is not the total mass of molecular gas but instead the denser molecular material that governs the level of star formation activity (e.g., Gao & Solomon 2004a; Lada et al. 2010). On the other hand, these results suggest that the analysis of the column density PDF and the denser gas fraction will provide us a diagnosis of the level of star formation activity in a molecular cloud.

5. Vertical Distribution

Warps and flares are common features in the outer disk of spiral galaxies. Early Galactic H I surveys have revealed warps that bend the Galactic disk upward in the first and second quadrants ($0° \leqslant l \leqslant 180°$) and downward in the third and fourth quadrants ($180° \leqslant l \leqslant 360°$; e.g., Westerhout 1957; Burton 1988; Voskes & Burton 1999). Furthermore, their amplitude increases with increasing galactic radius and varies strongly with Galactocentric azimuth (Kalberla & Kerp 2009). Besides H I, observational evidence for warping traced by molecular gas was obtained by many studies (e.g., Grabelsky et al. 1987; Clemens et al. 1988; Wouterloot et al. 1990; Burton & Liszt 1992). Using the whole-sky CO survey data of the CfA 1.2 m telescope, Nakanishi & Sofue (2006) completed a global analysis of the vertical distribution of Galactic CO emission. They found that the molecular gas disk exhibits a warp structure very similar to the atomic gas disk. Unfortunately, hampered by its relatively low sensitivity, the CO warp structure was only determined within a Galactocentric distance of 11 kpc (see Figures 11–12 of Nakanishi & Sofue 2006). With our new CO survey data with improved sensitivity, a new insight into the gas warp and flare is expected to be achieved in this Galactic longitude range of 130°–140°.

In order to get the vertical distribution of the molecular gas, we first measure the Z scale height on a pixel-by-pixel basis, defined by $Z = d \sin(b)$, where d is distance to the Sun and b is Galactic latitude. Second, we calculate the total mass of every 10 pc Z scale height. Then we can get the H_2 mass distribution along the Z scale height (Figure 14). The solid and dashed lines show the distributions in the region with detectable ^{12}CO (mask "B") and ^{13}CO (mask "G") emission, respectively. Interarm1 and Interarm2 are not considered here given their negligible contributions to the total molecular gas mass. The masses of the Local and Perseus arms are divided by 10 and 20, respectively, in order to plot them on the same scale as the Outer and OSC arms and facilitate comparison.

Here we should note that the Galactic latitude coverage of the MWISP survey almost fully covers the molecular gas emitted from the four segments of spiral arms, except for the nearest spiral arm, the Local arm, which shows an abrupt cutoff near $Z \approx 80$ pc, as shown in Figure 14. Therefore, we would expect a wider range of Z value once we fully cover emission from the Local arm by extending the Galactic latitude coverage range of the observation. Nevertheless, these issues have little effect on our overall results, given that the height and thickness of the Galactic disk near the Sun at a radius of 8–9 kpc were estimated to be ∼50 pc (see Figures 11–12 of Nakanishi & Sofue 2006).

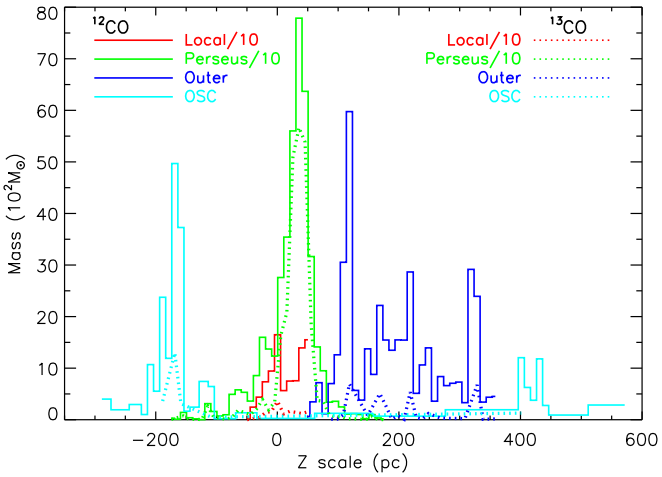

Figure 14. Molecular gas distributions of the Local (red), Perseus (green), Outer (blue), and OSC (cyan) arms along the Z scale. The distributions of ^{12}CO emission (mask "B") and ^{13}CO emission (mask "G") are indicated by solid and dashed lines, respectively. The masses of the Local and Perseus arms are divided by 10.

We find that the total mass, including both the diffuse and relatively dense gas components, usually has multiple distribution peaks, as shown by the solid lines. As expected, the mass of the denser gas component is more centrally concentrated at the most significant distribution peak of the total gas, as shown by the dashed lines. Considering that the arising of multiple components may make the thickness and height of a spiral arm obtained by applying a commonly used method of single Gaussian component fitting highly dubious, we do not attempt to fit the distributions.

It is obvious that the four arms exhibit different distributions in Figure 14. Although not perfect, the masses of the Local (peaked at ∼0 pc) and Perseus arms (peaked at ∼40 pc) are mainly concentrated at the middle of the Galactic plane, the $Z = 0$ plane. In contrast, the Outer arm peaked at ∼120 pc is apparently above the Galactic plane, and the OSC arm peaked at ∼−170 pc is mainly below the Galactic plane. Such a vertical displacement would faithfully reflect the warp of the outer Galactic gas disk, which might start at a place between the Perseus arm and the Outer arm in this region. In addition, the Local and Perseus arms are generally distributed within a much narrower range of Z scale than the OSC and Outer arms. This indicates that flare in the Local and Perseus arms is less obvious than in the Outer and OSC arms. Furthermore, because the latter two arms have a much larger distance both from the Sun and from the Galactic center, these results also suggest the increasing of thickness and scale height of a spiral arm with the Galactic radii, which is consistent with the results traced by H I, dust, and stellar emission (e.g., Drimmel & Spergel 2001; Momany et al. 2006).

6. Summary

Data from the MWISP Survey Project within Galactic coordinates $l = [129.^\circ75, 140.^\circ25]$ and $b = [-5.^\circ25, +5.^\circ25]$

have been presented. The $J = 1$–0 ^{12}CO, ^{13}CO, and C^{18}O lines were observed simultaneously using the PMODLH 13.7 m telescope. Thus, for the full $10.^{\circ}5 \times 10.^{\circ}5$ region sampled at 30″, there are 1,590,120 spectra for each isotopologue. In this study, we focus on the large-scale structures and their physical properties traced by ^{12}CO, ^{13}CO, and C^{18}O emission. The current massive star-forming sites traced by H II region and interstellar masers are also examined from the literature. The relations between the molecular gas properties and star formation activity are discussed. We also present the vertical distribution of molecular gas traced by the ^{12}CO and ^{13}CO emission in this Galactic range. The main results of this study are summarized as follows:

(1) The new data with the highest sensitivity and highest spatial dynamic range to date successively trace the molecular gas components of the distant arms (the Outer and the Outer Scutum Centaurus arms) and the internal substructures of the relatively nearby arms (the Local and Perseus arms) in this Galactic direction for the first time.

(2) We determine the column density, mass, surface gas density, and mass ratios between different isotopologues of each spiral arm and inter-arm. The physical properties change in different spiral arms and inter-arms and in different mask regions. The total H_2 masses of the mapped area traced by ^{12}CO, ^{13}CO, and C^{18}O emission are estimated to be 5.7×10^5, 2.7×10^5, and $3.4 \times 10^4\,M_{\odot}$, respectively. A large fraction of the observed molecular gas is found to be emitted from regions with low excitation temperature and low column density.

(3) Our review of the literature provides evidence for significant variations of the level of massive star formation activity in different spiral arms and inter-arms. A comparative study reveals that the level of star formation activity seems to be largely independent of the amount of total molecular gas mass traced by ^{12}CO, but it is closely related to the amount of relatively denser gas traced by ^{13}CO or C^{18}O and the column density PDF.

(4) The majority of the H_2 mass (about 70%) and massive star formation (about 90%) are found to be contributed by the Perseus arm, which suggests that the Perseus arm is a dominant spiral arm in this Galactic range.

(5) A large fraction of the observed total molecular gas originates from spiral arms. The mass contrasts between the adjacent spiral arms and inter-arms are found to be as high as 63 and 283 as traced by ^{12}CO and ^{13}CO, respectively. The denser gas components traced by ^{13}CO emission are more likely confined to the spiral arms than the relatively diffuse gas components traced by ^{12}CO emission. Moreover, the C^{18}O emission is exclusively distributed along the spiral arms. Therefore, we suggest that ^{13}CO and C^{18}O molecular lines are better arm tracers than the ^{12}CO molecular line, especially for those nearby arms.

(6) The vertical distributions of the ^{12}CO and ^{13}CO emission reveal a relatively flat and thin gas disk within the Perseus arm, while the disk appears warped and flared for regions beyond the Perseus arm.

We are grateful to all of the staff members of the Delingha 13.7 m radio telescopes for their support of the observations. We would like to thank the anonymous referee for the helpful comments and suggestions that helped to improve the paper. This work is supported by the National Key Research & Development Program of China (grant No. 2017YFA0402700), Key Research Program of Frontier Sciences, CAS (grant No. QYZDJ-SSW-SLH047), National Natural Science Foundation of China (grant Nos. 11773077, 11873019, 11673066, 11803091, and 11629302), and the Key Laboratory for Radio Astronomy, CAS, the Youth Innovation Promotion Association, CAS (2018355).

ORCID iDs

Yan Sun https://orcid.org/0000-0002-3904-1622
Ji Yang https://orcid.org/0000-0001-7768-7320
Shaobo Zhang https://orcid.org/0000-0003-2549-7247
Yang Su https://orcid.org/0000-0002-0197-470X
Hongchi Wang https://orcid.org/0000-0003-0746-7968
Xin Zhou https://orcid.org/0000-0003-2418-3350

References

Anderson, L. D., Armentrout, W. P., Johnstone, B. M., et al. 2015, ApJS, 221, 26
Anderson, L. D., Bania, T. M., Balser, D. S., et al. 2014, ApJS, 212, 1
Asaki, Y., Deguchi, S., Imai, H., et al. 2010, ApJ, 721, 267
Barnes, P. J., Hernandez, A. K., Muller, E., & Pitts, R. L. 2018, ApJ, 866, 19
Barnes, P. J., Muller, E., Indermuehle, B., et al. 2015, ApJ, 812, 6
Bieging, J. H., & Peters, W. L. 2011, ApJS, 196, 18
Bolatto, A. D., Wolfire, M., & Leroy, A. K. 2013, ARA&A, 51, 207
Bourke, T. L., Garay, G., Lehtinen, K. K., et al. 1997, ApJ, 476, 781
Brand, J., & Blitz, L. 1993, A&A, 275, 67
Brand, J., Cesaroni, R., Caselli, P., et al. 1994, A&AS, 103, 541
Breen, S. L., Ellingsen, S. P., Johnston-Hollitt, M., et al. 2007, MNRAS, 377, 491
Brunt, C. M. 2015, MNRAS, 449, 4465
Burton, W. B. 1988, in The Structure of our Galaxy Derived from Observations of Neutral Hydrogen, ed. K. I. Kellermann & G. L. Verschuur (New York: Springer), 295
Burton, W. B., & Liszt, H. S. 1992, A&AS, 95, 9
Carpenter, J. M., Heyer, M. H., & Snell, R. L. 2000, ApJS, 130, 381
Caswell, J. L., & Breen, S. L. 2010, MNRAS, 407, 2599
Clemens, D. P., Sanders, D. B., & Scoville, N. Z. 1988, ApJ, 327, 139
Comoretto, G., Palagi, F., Cesaroni, R., et al. 1990, A&AS, 84, 179
Dame, T. M., Elmegreen, B. G., Cohen, R. S., & Thaddeus, P. 1986, ApJ, 305, 892
Dame, T. M., Hartmann, D., & Thaddeus, P. 2001, ApJ, 547, 792
Digel, S. W., Lyder, D. A., Philbrick, A. J., Puche, D., & Thaddeus, P. 1996, ApJ, 458, 561
Drimmel, R., & Spergel, D. N. 2001, ApJ, 556, 181
Du, X., Xu, Y., Yang, J., & Sun, Y. 2017, ApJS, 229, 24
Feigelson, E. D., & Townsley, L. K. 2008, ApJ, 673, 354
Feldmann, R., Gnedin, N. Y., & Kravtsov, A. V. 2012, ApJ, 747, 124
Fich, M., & Blitz, L. 1984, ApJ, 279, 125
Foster, T., & Brunt, C. M. 2015, AJ, 150, 147
Frerking, M. A., Langer, W. D., & Wilson, R. W. 1982, ApJ, 262, 590
Gao, Y., & Solomon, P. M. 2004a, ApJS, 152, 63
Gao, Y., & Solomon, P. M. 2004b, ApJ, 606, 271
Garden, R. P., Hayashi, M., Gatley, I., Hasegawa, T., & Kaifu, N. 1991, ApJ, 374, 540
Georgelin, Y. M., & Georgelin, Y. P. 1976, A&A, 49, 57
Goldsmith, P. F., Heyer, M., Narayanan, G., Snell, R., Li, D., & Brunt, C. 2008, ApJ, 680, 428
Gong, M., Ostriker, E. C., & Kim, C.-G. 2018, ApJ, 858, 16
Grabelsky, D. A., Cohen, R. S., Bronfman, L., Thaddeus, P., & May, J. 1987, ApJ, 315, 122
Green, J. A., Breen, S. L., Fuller, G. A., et al. 2017, MNRAS, 469, 1383
Heyer, M., & Dame, T. M. 2015, ARA&A, 53, 583
Heyer, M., Krawczyk, C., Duval, J., & Jackson, J. M. 2009, ApJ, 699, 1092
Heyer, M. H., Brunt, C., Snell, R. L., et al. 1998, ApJS, 115, 241
Hou, L. G., & Han, J. L. 2014, A&A, 569, A125
Hou, L. G., Han, J. L., & Shi, W. B. 2009, A&A, 499, 473
Hughes, V. A., & Viner, M. R. 1982, AJ, 87, 685
Humphreys, R. M. 1978, ApJS, 38, 309
Izumi, N., Kobayashi, N., Yasui, C., et al. 2014, ApJ, 795, 66
Jackson, J. M., Rathborne, J. M., Shah, R. Y., et al. 2006, ApJS, 163, 145
Kainulainen, J., Beuther, H., Banerjee, R., Federrath, C., & Henning, T. 2010, A&A, 530, 64
Kalberla, P. M. W., & Kerp, J. 2009, ARA&A, 47, 27

Koda, J., Scoville, N., Sawada, T., et al. 2009, ApJL, 700, L132
Kong, S., Lada, C. J., Lada, E. A., et al. 2015, ApJ, 805, 58
Kramer, C., Jakob, H., Mookerjea, B., et al. 2004, A&A, 424, 887
Lada, C. J., Elmegreen, B. G., Cong, H. I., & Thaddeus, P. 1978, ApJL, 226, 39
Lada, C. J., Lombardi, M., & Alves, J. F. 2010, ApJL, 724, 687
Lee, Y., Stark, A. A., Kim, H.-G., & Moon, D.-S. 2001, ApJS, 136, 137
Li, Y. J., Xu, Y., Sun, Y., et al. 2019, ApJS, 242, 19
Lombardi, M., Lada, C. J., & Alves, J. 2010, A&A, 512, 67
Megeath, S. T., Townsley, L. K., Oey, M. S., & Tieftrunk, A. R. 2008, in Handbook of Star-forming Regions, Vol. 4, ed. B. Reipurth (Tucson, AZ: Univ. Arizona Press), 264
Milam, S. N., Savage, C., Brewster, M. A., Ziurys, L. M., & Wyckoff, S. 2005, ApJ, 634, 1126
Mizuno, A., & Fukui, Y. 2004, in ASP Conf. Ser. 317, Milky Way Surveys: The Structure and Evolution of our Galaxy, ed. D. Clemens, R. Shah, & T. Brainerd (San Francisco, CA: ASP), 59
Momany, Y., Zaggia, S., Gilmore, G., et al. 2006, A&A, 451, 515
Moore, T. J. T., Bretherton, D. E., Fujiyoshi, T., et al. 2007, MNRAS, 379, 663
Nakanishi, H., & Sofue, Y. 2006, PASJ, 58, 847
Nakano, M., Soejima, T., Chibueze, J. O., et al. 2017, PASJ, 69, 16
Narayanan, G., Heyer, M., Brunt, C., et al. 2008, ApJS, 177, 341
Pestalozzi, M. R., Minier, V., & Booth, R. S. 2005, A&A, 432, 737
Pety, J. 2005, in Semaine de l'Astrophysique Francaise, SF2A-2005, ed. F. Casoli et al. (Les Ulis: EdP Sciences), 721
Pineda, J. E., Caselli, P., & Goodman, A. A. 2008, ApJ, 679, 481
Polychroni, D., Moore, T. J. T., & Allsopp, J. 2012, MNRAS, 422, 2992
Reid, M. J., Menten, K. M., Brunthaler, A., et al. 2014, ApJ, 783, 130
Ridge, N. A., Schnee, S. L., Goodman, A. A., & Foster, J. B. 2006, ApJ, 643, 932
Ruch, G. T., Jones, T. J., Woodward, C. E., et al. 2007, ApJ, 654, 338
Russeil, D., Adami, C., & Georgelin, Y. M. 2007, A&A, 470, 161
Sakai, T., Oka, T., & Yamamoto, S. 2007, ApJ, 662, 1043
Schinnerer, E., Meidt, S. E., Pety, J., et al. 2013, ApJ, 779, 42
Shan, W. L., Yang, J., Shi, S. C., et al. 2012, ITTST, 2, 593
Sheffer, Y., Rogers, M., Federman, S. R., et al. 2008, ApJ, 687, 1075
Shimajiri, Y., Kitamura, Y., Nakamura, F., et al. 2015, ApJS, 217, 7
Straižys, V., & Laugalys, V. 2007, BaltA, 16, 167
Straižys, V., & Laugalys, V. 2008, in Handbook of Star-forming Regions, Vol. I, ed. B. Reipurth (San Francisco, CA: ASP), 294
Su, Y., Yang, J., Zhang, S. B., et al. 2019, ApJS, 240, 9
Sun, J. X., Lu, D. R., Yang, J., et al. 2018, AcASn, 59, 3
Sun, Y., Su, Y., Zhang, S.-B., et al. 2017, ApJS, 230, 17
Sun, Y., Xu, Y., Chen, X., et al. 2014, A&A, 563, 130
Sun, Y., Xu, Y., Chen, X., et al. 2018, ApJ, 869, 148
Sun, Y., Xu, Y., Yang, J., et al. 2015, ApJL, 798, L27
Szymczak, M., Pillai, T., & Menten, K. M. 2005, A&A, 434, 613
Titmarsh, A. M., Ellingsen, S. P., Breen, S. L., Caswell, J. L., & Voronkov, M. A. 2014, MNRAS, 443, 2923
Titmarsh, A. M., Ellingsen, S. P., Breen, S. L., Caswell, J. L., & Voronkov, M. A. 2016, MNRAS, 459, 157
Torii, K., Fujita, S., Nishimura, A., et al. 2019, PASJ, 71, S2
Turner, D. G., & Evans, N. R. 1984, ApJ, 283, 254
Umemoto, T., Minamidani, T., Kuno, N., et al. 2017, PASJ, 69, 78
Urquhart, J. S., Hoare, M. G., Lumsden, S. L., et al. 2009, A&A, 507, 795
Valdettaro, R., Palla, F., Brand, J., et al. 2001, A&A, 368, 845
van Dishoeck, E. F., & Black, J. H. 1988, ApJ, 334, 771
Voskes, T., & Burton, W. B. 1999, in ASP Conf. Ser. 168, New Perspectives on the Interstellar Medium, ed. A. R. Taylor, T. L. Landecker, & G. Joncas (San Francisco, CA: ASP), 375
Walsh, A. J., Breen, S. L., Britton, T., et al. 2011, MNRAS, 416, 1764
Wang, C., Yang, J., Su, Y., et al. 2019, ApJS, 243, 25
Weaver, H. 1974, in IAU Symp. 60, Galactic Radio Astronomy, ed. F. J. Kerr & S. C. Simonson (Cambridge: Cambridge Univ. Press), 573
Westerhout, G. 1957, BAN, 13, 201
Wilson, R. W., Jefferts, K. B., & Penzias, A. A. 1970, ApJ, 161, 43
Wilson, T. L., & Rood, R. 1994, ARA&A, 32, 191
Wouterloot, J. G. A., Brand, J., Burton, W. B., & Kwee, K. K. 1990, A&A, 230, 21
Wu, J., Evans, N. J., Gao, Y., et al. 2005, ApJL, 635, 173
Wu, J., Evans, N. J., Shirley, Y. L., & Knez, C. 2010, ApJS, 188, 313
Xi, H., Zhou, J., Esimbek, J., et al. 2015, MNRAS, 453, 4203
Xi, H.-W., Zhou, J.-J., Esimbek, J., et al. 2016, RAA, 16, 89
Xu, Y., Li, J. J., Hachisuka, K., et al. 2008, A&A, 485, 729
Xu, Y., Reid, M. J., Zheng, X. W., & Menten, K. M. 2006, Sci, 311, 54
Yang, J., Jiang, Z. B., Wang, M., Ju, B. G., & Wang, H. C. 2002, ApJS, 141, 157
Yang, K., Chen, X., Shen, Z. Q., et al. 2017, ApJ, 846, 160
Zhang, S., Xu, Y., & Yang, J. 2014, AJ, 147, 46
Zhou, X., Yang, J., Fang, M., et al. 2016, ApJ, 833, 4